

Cherenkov light-based beam profiling for ultrarelativistic electron beams

E. Adli^{a,b}, S.J. Gessner^b, S. Corde^b, M.J. Hogan^b, H.H. Bjerke^{b,c}

^a*Department of Physics, University of Oslo, N-0316 Oslo, Norway*

^b*SLAC National Accelerator Laboratory, 2575 Sand Hill Road, Menlo Park, California 94025, USA*

^c*Department of Physics, Norwegian University of Science and Technology, N-7491 Trondheim, Norway*

Abstract

We describe a beam profile monitor design based on Cherenkov light emitted from a charged particle beam in an air gap. The main components of the profile monitor are silicon wafers used to reflect Cherenkov light onto a camera lens system. The design allows for measuring large beam sizes, with large photon yield per beam charge and excellent signal linearity with beam charge. The profile monitor signal is independent of the particle energy for ultrarelativistic particles. Different design and parameter considerations are discussed. A Cherenkov light-based profile monitor has been installed at the FACET User Facility at SLAC. We report on the measured performance of this profile monitor.

Keywords: electron beams, profile monitor, Cherenkov light, FACET User Facility

1. Introduction

For a number of accelerator facilities there is a need for precise diagnostic methods for measuring the transverse beam profile of ultrarelativistic electron beams with large transverse sizes, for example beams with large energy spread in a spectrometer line. These types of spectrometers may be required in various branches of advanced accelerator experiments like plasma wake

Email address: Erik.Adli@fys.uio.no (E. Adli)

Preprint submitted to Nuclear Physics A

January 12, 2015

field acceleration [1], laser plasma acceleration [2], and two-beam acceleration machines where drive beams are heavily decelerated with large energy spread, such as CLIC [3].

We present here a beam profile diagnostic method based on Cherenkov light generated by an electron beam traveling through air. The profile monitor works equally well for electrons and positrons. This type of diagnostic was first used for plasma experiments at the SLAC Final Focus Test Beam Facility [4, 5] and has been further developed for the spectrometer at the FACET User Facility [1, 6], as described in this paper.

The use of Cherenkov radiation for profile monitoring has the significant advantage over the more established use of optical transition radiation (OTR), in that the light yield per beam electron may be much larger. Cherenkov radiation in air generates on the order of 30 photons per electron per meter, in the optical range (shown below). In comparison the OTR energy spectrum, $dW_{\text{otr}}/d\omega$, from relativistic electrons is approximately given by [7]

$$\frac{dW_{\text{otr}}}{d\omega} \approx 4.9 \times 10^{-37} \ln \gamma$$

where γ is the Lorentz factor, which yields about 0.05 OTR photons per electron per surface unit for ultrarelativistic beams, in the optical range. By using enough path length to generate Cherenkov light, one may easily get a factor 100 stronger signal with a detector based on Cherenkov light compared to an OTR-based setup. For beams with large energy spread, the Cherenkov light has the added advantage over OTR that the light yield is independent of the particle energy. High light yield is important in advanced accelerator experiments where small charge signals may be of great experimental interest, as illustrated for example by the low charge accelerated tail described in [4]. On the other hand, beams in the FACET experimental area may have very high charge densities, reaching on the order of 1000 nC/mm². The Cherenkov profile monitor has the advantage that the light yield is linear in charge over the full charge density range. Scintillating materials used for beam profiling, for example Kodak Lanex, also provide high light yield. These type of screens, however, may cease to be linear in charge at certain charge densities. In [8] several types of Lanex are reported to have a saturated signal at densities of less than 100 pC/mm², four orders of magnitude lower than the FACET peak charge density. Large charge density may also damage scintillating materials, while our setup based on Cherenkov radiation has proven resistant to damage, as reported later in this paper. Another

43 advantage of the Cherenkov profile monitor is that upstream photons, origi-
 44 nating from upstream beam interactions with beam line elements or, in our
 45 case, the plasma, will not generate Cherenkov radiation. The Cherenkov
 46 profile monitor can therefore separate the incoming electrons from incoming
 47 photons. Finally, as we will discuss, our profile monitor design provides the
 48 possibility of large field of views, and is a relatively robust and simple system
 49 to set up as well as a cost-effective solution for a profile monitor.

50 We first discuss general principles and parameter considerations. We
 51 then describe the design of the Cherenkov light-based profile monitor for the
 52 spectrometer for the FACET User Facility and report on its performance.

53 2. Principle

54 Charged particles traveling faster than the speed of light in a given
 55 medium emit Cherenkov radiation [9].

56 The index of refraction of dry air, n_{air} , can be estimated from the modified
 57 Edlén formulas [10, 11] and ranges from 1.000270 to 1.000278, at 20 deg C
 58 temperature and 1 atm. pressure, when the wavelength ranges from 400 nm
 59 to 750 nm. We will in this paper assume typical laboratory conditions where
 60 the air humidity, pressure and temperature do not change significantly, and
 61 assume the index of refraction to $n_{\text{air}} = 1.000274 \pm 0.000004$. We assume
 62 thus the speed of light in air, $v_{\text{air}} = c/n_{\text{air}}$, to be constant. Particles with
 63 normalized velocity $\beta = v/c$ greater than $1/n_{\text{air}}$ will emit Cherenkov radia-
 64 tion. For electrons, this corresponds to an energy of 21 MeV or more. The
 65 opening angle of the resulting Cherenkov radiation is given by

$$\cos \theta = \frac{1}{n_{\text{air}} \beta}.$$

66 We note that for electrons with energy of 150 MeV or more, the opening
 67 angle will be within 1% of the opening angle for infinite energy,

$$\theta_C = \cos^{-1}(1/n_{\text{air}}) = 24.2 \text{ mrad}.$$

68 In this paper we are mostly concerned with ultrarelativistic electrons and we
 69 assume for calculations the opening angle to be that of infinite energy, θ_C .
 70 For this energy range, the Cherenkov profile monitor has the advantage that
 71 the signal intensity is for our purposes independent of the particle energy.

72 The Cherenkov radiation frequency spectrum is given by the Frank-Tamm
 73 formula [12], which yields the number of photons, N , emitted per unit length,
 74 dx , and wavelength interval, $d\lambda$,

$$\frac{d^2 N}{d\lambda dx} = \frac{2\pi\alpha}{\lambda^2} \sin^2 \theta_C, \quad (1)$$

75 where $\alpha \approx 1/137$ is the fine-structure constant. We are interested in the
 76 frequency range corresponding to the sensitive range of the cameras used the
 77 experimental setup, which in our case is from about 400 nm to about 750
 78 nm. Using Eq. (1) we calculate the number of photons per electron per unit
 79 length, generated in this frequency range, to

$$\frac{dN}{dx} = 2\pi\alpha \sin^2 \theta_C \int_{400nm}^{750nm} \frac{d\lambda}{\lambda^2} = 29 \text{ m}^{-1}. \quad (2)$$

80 In order to control the amount of photons generated, the electron beam
 81 to be profiled passes through two wafers as it travels through air. The first
 82 wafer blocks light already generated up to this point, and the second wafer
 83 reflects the light generated between the two wafers. The total number of
 84 photons can be regulated by adjusting the gap between the two wafers, d_{gap} .
 85 We require a wafer material that has good reflectivity in the optical range, as
 86 well as a high damage threshold. We have chosen silicon, which reflects about
 87 30-40% of incident light. Silicon wafers have the advantage that they can be
 88 procured off-the-shelf in appropriate shapes and thicknesses for a reasonable
 89 price.

90 In order to image the beam, a standard CCD camera and a commercial
 91 lens may be used, adjusted to point-to-point focus from the center of the
 92 air gap onto the camera sensor. In order to image an electron, the electron
 93 position must be in the field of view of the camera and either all light emitted,
 94 or a fraction of the light emitted, must hit the camera lens. Figure 1 a)
 95 illustrates how the profile monitor can be set up.

96 3. Parameter considerations

97 We now discuss a few key considerations particular to the Cherenkov pro-
 98 file monitor which are required to optimize the profile monitor performance.

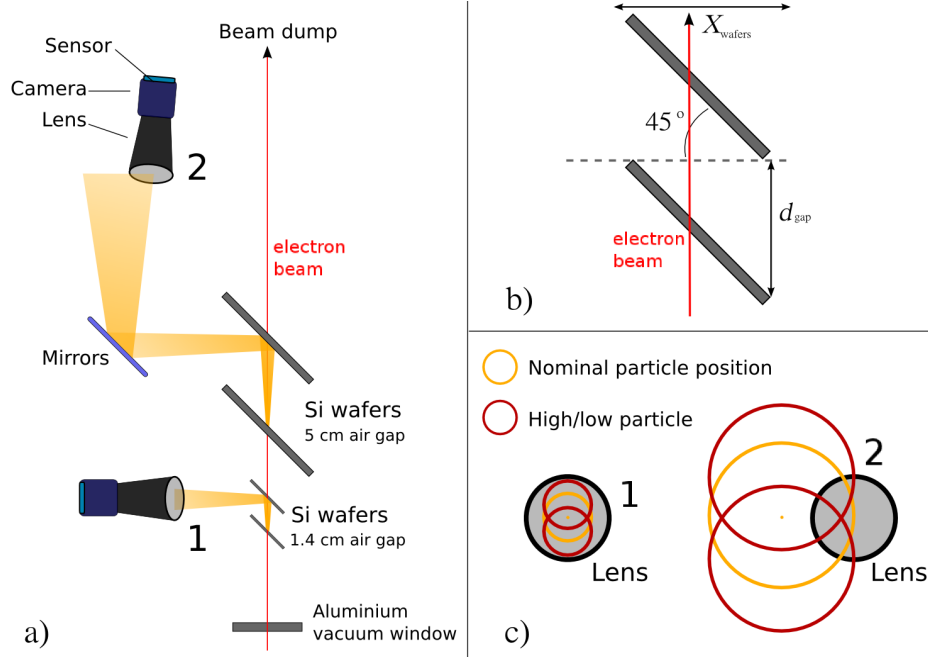


Figure 1: Illustration of a Cherenkov light-based profile monitor setup. An ultrarelativistic electron beam enters air, and emits Cherenkov radiation. A first silicon wafer blocks upstream light, while a second silicon wafer reflects the light generated between the two wafers onto a lens. Apart from scattering in the Si, the profile monitors are non-intrusive and several monitors might be used simultaneously. a) shows a schematic overview of the FACET Cherenkov spectrometer profile monitor setup. Parameters for this setup will be discussed later in the paper. b) shows a possible geometry for the wafer setup. c) shows the principles of the two modes of operation, where either all the Cherenkov light is collected on the lens (marked with “1”), or, only a fraction of the ring is collected on the lens (marked with “2”).

99 3.1. Length of air gap versus resolution limitations

100 One contribution to the detector resolution is given by the fact that the
 101 Cherenkov light is emitted continuously along a finite air gap. To estimate
 102 the resolution limit due to the air gap we use a ray tracing model assuming
 103 linear optics. In this model the light emitted from a certain distance upstream
 104 or downstream of the focal plane will form a ring on the camera sensor,
 105 equivalent to a depth of field circle of confusion. Each longitudinal slice along
 106 the air gap give origin to rings with different radii. We assume that the lens
 107 is set to focus in the middle of the air gap, at longitudinal position $z=0$.
 108 At the camera sensor, the radius of the rings originating at a longitudinal
 109 distance $\pm z$ from the focus are given by $r_{\text{sensor}}(z) = mz \tan(\theta_C)$, where m
 110 is the lens magnification. The intensity per pixel of the rings decreases as
 111 $1/r_{\text{sensor}}$ since the same number of photons is spread out over a larger area.
 112 In order to compare the depth of field effect with the size of the beam to be
 113 imaged, we are interested in the corresponding size of the rings in the focal
 114 plane, given by $r(z) = r_{\text{sensor}}(z)/m = z \tan(\theta_C)$. The net effect is that an
 115 infinitely thin electron beam will be observed as having a finite thickness. In
 116 Figure 2 we calculate this distribution for a 5 cm long air gap, where the lens
 117 focus is in the middle of the gap. The distribution rms width in the focal
 118 plane is in this case 155 μm .

119 The blocking and the reflecting wafers must be rotated by the same angle
 120 in order not to generate correlation between beam transverse position and
 121 signal intensity. Placing the wafers at 45 degree angle with respect to the
 122 beam trajectory minimizes the length of the air gap with respect to the
 123 projected width of the wafers in the plane orthogonal to the beam trajectory.
 124 The minimum length of the air gap is therefore given by the projected width
 125 of the wafers, $d_{\text{gap}} \geq X_{\text{wafers}}$, as illustrated in Figure 1 b). An important
 126 system design trade-off is therefore the resolution limitations originating from
 127 the air gap depth-of-field error, versus transverse field of view limitations
 128 from the projected wafer width. The air gap may be made larger than the
 129 projected wafer width, if it is desired to increase the camera signal level, as
 130 the photon yield increases linearly with the air gap.

131 3.2. Field of view versus fraction of collected light

132 The Cherenkov radiation is propagating in a cone with opening angle θ_C .
 133 This can be exploited to image a field of view (FOV) much larger than the
 134 lens itself, because only a fraction of the Cherenkov ring needs to be captured
 135 in order to image the emitting charge. We first discuss the simpler case, where

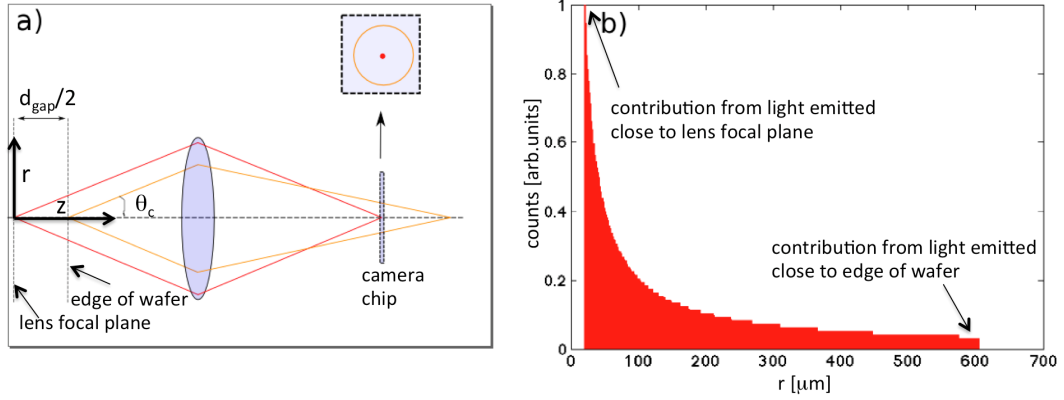


Figure 2: (a) Principle of the depth of field blurring due to Cherenkov light emitted away from the focal plane of the camera system, calculated using a ray tracing model. Photons emitted a distance $\pm z$ away from the focal plane will form rings on the sensor, with the corresponding ring radius in the focal plane given by $r(z) = z \tan(\theta_C)$. (b) The corresponding intensity distribution in the focal plane, after an infinitely thin electron beam has passed through an air gap of 5 cm. Photons originating at the focus in the middle of the air gap are imaged at the center pixel at $r = 0$. Photons generated upstream or downstream of the focus are spread out in rings with intensity proportional to $1/r$ yielding the distribution shown in the figure. The rings with the largest radius originate from light emitted when the electrons pass close to the wafer edge. In the focal plane this corresponds to rings with radius $r = 2.5 \text{ cm} \times \tan(\theta_C) = 600 \mu\text{m}$. The distribution rms width in the focal plane is in this case $155 \mu\text{m}$. The granularity of this calculation corresponds to the FACET camera pixel size.

136 the lens captures the entire ring for the desired FOV, as illustrated in Figure
 137 1 c) 1. In this case the Cherenkov light signal is distributed onto the imaging
 138 sensor proportional to the electron charge. The maximum effective FOV of
 139 the camera is limited to the lens diameter $2r_{\text{lens}}$ minus the diameter of the
 140 Cherenkov ring at the position of the lens, $2r_{\text{ring}} = 2s\theta_C$, where we define s
 141 as the distance from the center of the wafers to the lens. In order to image
 142 the full FOV, the optical magnification factor, $m = f/(s - f)$, where f is the
 143 focal length of the lens, must be $m \leq X/(2r_{\text{lens}} - 2r_{\text{ring}})$, assuming a square
 144 sensor with width X ; see Figure 1 b). A smaller magnification would not be
 145 useful, as the light would not be collected by the lens. A larger magnification
 146 may be useful to increase the resolution, if the depth-of-field error is not a
 147 limiting factor, which again depends on the air gap, as discussed above.

148 As an alternative mode of operation, the profile monitor can be designed
 149 such that only a fraction of the Cherenkov ring hits the lens. The corre-
 150 sponding setup is illustrated in Figure 1 c) 2, for a case where the Cherenkov
 151 ring radius is several times larger than the lens radius. This mode of opera-
 152 tion has the significant advantage that the FOV in one plane can be as large
 153 as desired, limited only by wafer sizes and resolution limits. One possible
 154 use of this mode of operation is for energy spectrum measurement where the
 155 electron beam is highly dispersed according to its energy in one plane. The
 156 fraction of the Cherenkov light ring that hits the lens depends on the position
 157 of the charge imaged, as illustrated in Figure 1 c). In order to optimize the
 158 system performance we calculate the fraction of light collected for the desired
 159 FOV. To find a general expression, we use Figure 3, where D is the distance
 160 from the center of the lens to the center of the Cherenkov ring, and r_{lens} and
 161 r_{ring} are the radii of the lens and the Cherenkov ring respectively.

162 The intersection of the two rings in Figure 3 along the horizontal axis is
 163 calculated as

$$\xi = \frac{D^2 - r_{\text{lens}}^2 + r_{\text{ring}}^2}{2D}$$

164 and along the vertical axis as

$$\psi^2 = \frac{4D^2r_{\text{ring}}^2 - (D^2 - r_{\text{lens}}^2 + r_{\text{ring}}^2)^2}{4D^2}.$$

165 The full angle of the Cherenkov ring inside the intersections is given by

$$\alpha = 2 \arctan \frac{\psi}{\xi}.$$

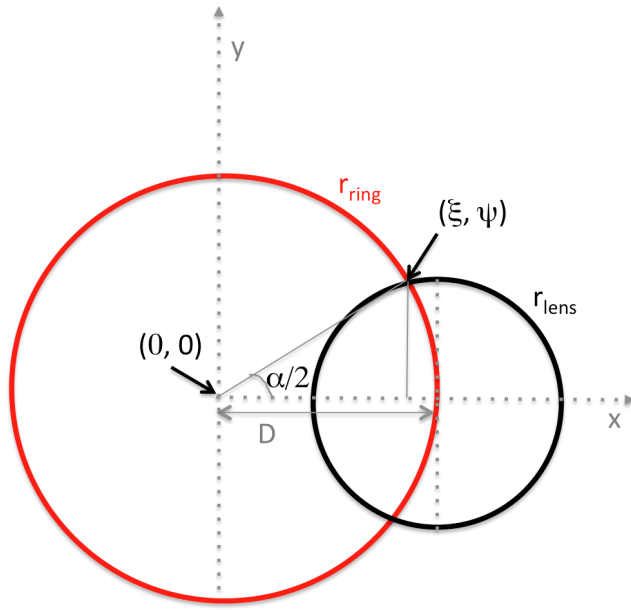


Figure 3: If the camera lens is put far enough from the air gap, the Cherenkov ring (red) will have a larger radius than the radius of the lens (black). The fraction of light falling on the lens and being imaged on the sensor will depend on the horizontal and vertical position of the emitting charge. By optimizing the ring radii and the distance between the Cherenkov ring and the lens, the variation in the fraction of light falling on the lens can be kept relatively small over the entire field of view.

166 It follows that the fractional light yield from a particle for which the Cherenkov
 167 ring has a center at a transverse distance D from the lens center, is given by

$$p_{light} = \frac{\alpha}{2\pi} = \frac{1}{\pi} \arctan \frac{\sqrt{4D^2 r_{ring}^2 - (D^2 - r_{lens}^2 + r_{ring}^2)^2}}{D^2 - r_{lens}^2 + r_{ring}^2}. \quad (3)$$

168 For charge which at the object plane is offset with respect to the particle
 169 with its ring at a distance D , the fraction of the light can be calculated by
 170 substituting D in Eq. (3) by

$$D_{charge}(x, y) = \sqrt{(D - x)^2 + y^2}, \quad (4)$$

171 where x is the offset in the horizontal dimension and y the offset in the
 172 vertical dimension. Eqs. (3) and (4) can be used to calculate the variation
 173 in light yield across the camera FOV. Typically, one would like good light
 174 yield in the center of the FOV, though there may be less light yield towards
 175 the edges of the FOV. We will refer to this effect as “vignetting”.

176 In the limit where the lens is placed very far away from the wafers such
 177 that $r_{ring} \gg r_{lens}$, and where the Cherenkov ring center is at a distance
 178 $D = r_{ring}$ from the lens center, the light yield can be approximated by

$$p_{light} = \frac{1}{\pi} \frac{r_{lens}}{r_{ring}} \sqrt{1 - x^2}. \quad (5)$$

179 In this case any imaged particle with zero horizontal position will have the
 180 same light yield; the vignetting does not depend on vertical position. The
 181 part of the beam which can be imaged is limited only by the camera FOV and
 182 the wafer size. In the horizontal plane it falls off when the almost straight
 183 lines of the Cherenkov rings move towards the edges of the lens. To achieve
 184 constant light yield over a large range, in one dimension, a configuration
 185 with the lens far away may thus be used. The focal length of the lens must
 186 be comparably large in order to optimize the magnification for the camera
 187 sensor size. As an example we illustrate the vignetting effect for the case
 188 of $r_{ring} \gg r_{lens}$, where a lens with radius $r_{lens} = 7.5$ cm and a focal length
 189 of $f = 600$ mm is placed a distance $s = 20$ m away from the wafer. The
 190 Cherenkov rings have a radius of $r_{ring} = \theta_C s = 48$ cm at this distance. Figure
 191 4 shows the vignetting effects for this configuration, assuming the distance
 192 between the ring and the lens is set to $D = r_{ring}$, calculated using Eqs. (3)
 193 and (4). The FOV shown corresponds to a camera sensor size of 14×17

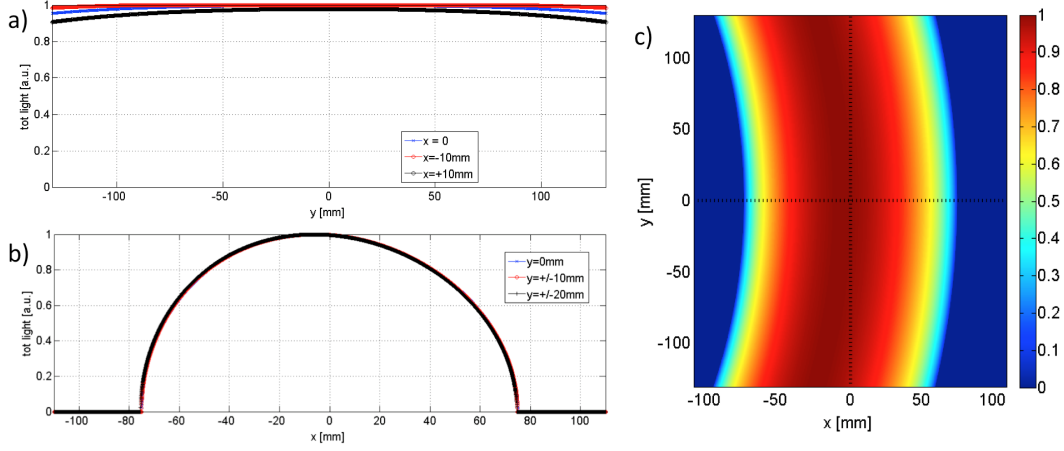


Figure 4: An example calculation of the vignetting effects for the case where the Cherenkov ring radius is larger than the lens radius. The lens has a radius of 7.5 cm and is placed 20 m away from the silicon wafers. The resulting Cherenkov ring radius is 48 cm. The figures are calculated using Eqs. (3) and (4). (a) Along the vertical axis, the light yield varies by only up to $\pm 2.5\%$, over a range of 20 cm. (b) In the horizontal dimension, the light yield follows Eq. (5) closely. (c) A two-dimensional calculation of the light yield as function of both horizontal and vertical charge locations.

mm², and we have assumed that the wafers cover the entire FOV. We observe that on the horizontal axis the variation in light yield is $\pm 2.5\%$ up to y values of ± 13 cm. On the $y = 0$ axis the light yield is limited by the lens radius, and closely follows Eq. (5).

4. Experimental setup at FACET

Practical systems will be limited by the lenses and cameras available as well as physical boundaries. We describe here the experimental setup of a Cherenkov light-based profile monitor installed at the FACET User Facility, as part of the FACET imaging spectrometer. This setup is based on the principle of capturing a fraction of the Cherenkov light on the lens in order to access a large field of view in the energy-dispersed plane (vertical plane). The field of view captures particles decelerated to less than half the FACET nominal energy (20.35 GeV) and up to infinite energy. We first discuss the parameters for this system, then we compare calculated resolution and vignetting against measurements.

209 The FACET Cherenkov monitor is installed in the FACET tunnel, close
 210 to the beam dump, on an optics table with a footprint of $1.2 \times 2.4 \text{ m}^2$. A
 211 Nikkor lens with radius of $r_{\text{lens}} = 7.5 \text{ cm}$ and a focal length of $f = 600 \text{ mm}$
 212 is installed on a CMOS camera with a sensor size of $14.0 \times 16.6 \text{ mm}^2$. The
 213 CMOS camera is of type PCO.edge 5.5, with 16 bit dynamic range [13]. The
 214 lens aperture was fully opened, with an f-number of $f_{\#} = f/2r_{\text{lens}} = 4$. The
 215 camera lens was positioned $s = 5.9 \text{ m}$ away from the center of the wafers,
 216 using three high-quality 6" mirrors. The resulting magnification $m = 0.104$
 217 yields a FOV of $13.5 \times 16.0 \text{ cm}^2$. The resulting Cherenkov ring at the lens
 218 is $r_{\text{ring}} = \theta_C s = 14.3 \text{ cm}$. The air gap between the wafers is $d_{\text{gap}} = 5 \text{ cm}$.
 219 The distance from the center of the Cherenkov ring for the nominal energy
 220 particle, to the center of the lens, was set to $D = 0.84r_{\text{ring}} = 12.0 \text{ cm}$,
 221 optimized to give the minimum overall vignetting effects.

222 In addition to the Cherenkov radiation generated in the air gap, opti-
 223 cal transition radiation (OTR) is generated in the transition between the
 224 wafers and the air. From [7] we have estimated the OTR emission to about
 225 0.05 OTR photons per electron per surface, which is a few percent of the
 226 Cherenkov emission for our experimental setup. The intensity distribution
 227 of the transition radiation is very sharply peaked at an angle $\theta=1/\gamma$ [7], which
 228 in our experiment amounts to $\theta=0.049 \text{ mrad}$. However, in the experimental
 229 setup, the radiation narrowly emitted around this angle is not collected by
 230 the camera lens, since the lens is positioned at an offset with respect to the
 231 line of sight, $\theta=0$. We therefore expect no contributions from OTR in our
 232 profile monitor.

233 The CMOS camera is sensitive to wavelengths up to about 750 nm , which
 234 for $f_{\#} = 4$ gives a diffraction limit on the camera sensor of $1.22 \times 750 \text{ nm} \times$
 235 $f_{\#} = 3.7 \mu\text{m}$ and a diffraction limit on the target of $35 \mu\text{m}$. In comparison,
 236 the resolution of the optical system (CMOS camera + lens) was measured
 237 to be $88 \mu\text{m}$ using a 1951 USAF resolution test target [14], which is close to,
 238 and possibly dominated by, the pixel resolution of $62 \mu\text{m}$.

239 The beam enters the air from vacuum through a 5.1 mm thick aluminum
 240 window. The window is relatively thick since it is optimized for a large
 241 opening for the beam of 15 cm in the horizontal plane and 40 cm in the
 242 vertical plane. The rms multiple scattering angle from the window is $143 \mu\text{rad}$
 243 [15]. The Cherenkov wafers are located 86 cm downstream of the window,
 244 yielding a minimum beam spot size at the wafers of $122 \mu\text{m}$. The scatter
 245 from the wafers themselves has negligible effect on the minimum spot size.
 246 The experimental setup in the FACET tunnel is shown in Figure 5.

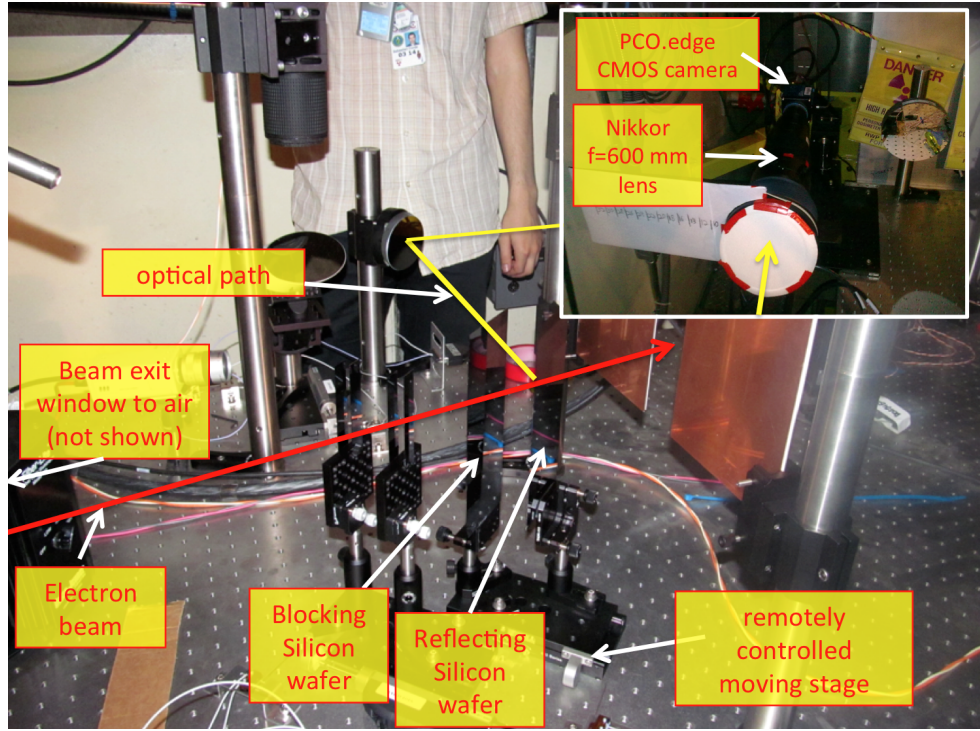


Figure 5: The experimental setup in the FACET tunnel. All components are installed on a $1.2\text{ m} \times 2.4\text{ m}$ optical table. The upper right inset depicts components installed in the upper right corner of the main picture. The electron beam, indicated in red, passes through two silicon wafers. The first wafer blocks the light generated upstream, while the second wafer reflects the light generated between the two wafers onto a Nikkor 600 mm 15 cm diameter lens, reflecting off three mirrors for a total path length of 6 m. Only part of the light path is indicated in the picture. The wafers can be moved in and out of the electron beam line, using a remotely controlled moving stage. In the picture there are also additional equipment related to other diagnostics, not described here.

247 5. Performance

248 We have tested the experimental setup described above, using the FACET
249 electron beam with a nominal charge of $2 \times 10^{10}e$ and a nominal energy of
250 20.35 GeV.

251 5.1. Sensitivity and linearity

252 Each camera pixel has a range of 2^{16} output values. We correlated the
253 camera signal level with the charge in the spectrometer line, measured using
254 a BPM. This yielded a sensitivity of 52 electrons or positrons per pixel output
255 value, corresponding to 75 photons per pixel output value, using Eq. (2). The
256 measurements were performed with relatively new wafers. In comparison, the
257 effective noise level of the system as installed in the FACET tunnel is about
258 5 bits (a value of 31). Thus, about 1600 electrons or positrons per pixel is
259 required to generate a signal above the noise level. The camera is fitted with
260 a retractable filter that decreases the sensitivity by a factor 70, in order to
261 avoid camera sensor saturation when the FACET beam has a small energy
262 spread. The measurements showed that the signal level is linear in charge
263 density, as expected. The data for the sensitivity calculation is shown in
264 Figure 6.

266 5.2. Vignetting

267 The FACET spectrometer profile monitor is optimized for a large field of
268 view, and for small vignetting effects. The large radius lens in combination
269 with the large distance between the silicon wafers and the lens leads to small
270 vignetting effects in the field of view, according to the ray tracing model,
271 as shown in Figure 4. We have experimentally measured the light yield in
272 a region of 2.4 cm in the horizontal by 5 cm in the vertical, and compared
273 it to the theoretical values predicted from Eq. (3). The measurements were
274 performed by moving the beam using correctors and dipole magnets in a $5 \times$
275 5 grid. Within the range documented here, the beam could be moved without
276 inducing significant losses during the transport to the dump. Figure 7 (top
277 row) shows the predicted values to the left, and the measured values to the
278 right. For the measured results, the nominal beam is centered on $x=0$ and
279 $y=0$. In both cases the light yield is within a few percent of the maximum,
280 showing that the vignetting effects in the profile monitor are indeed small.
281 In comparison, we also measured the vignetting with the lens iris partially

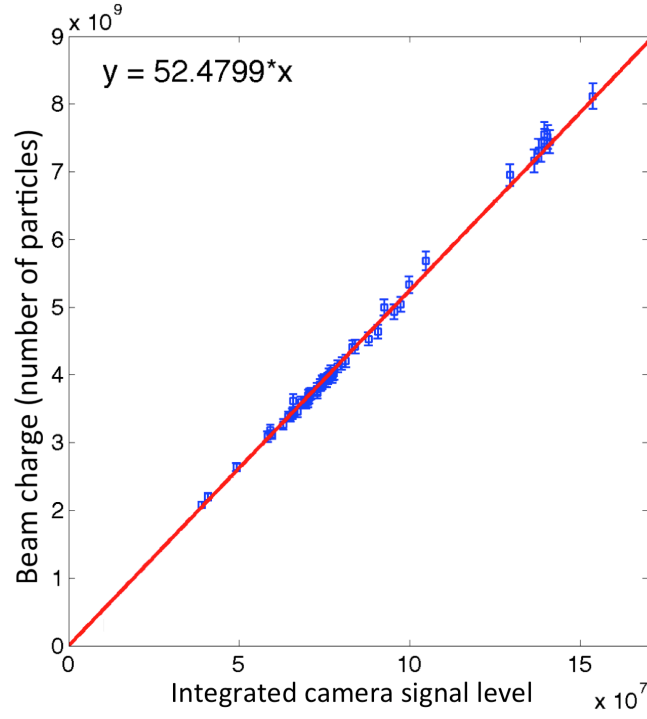


Figure 6: Integrated camera signal level correlated with beam position monitor (BPM) signal level, for a beam of up to 8×10^9 positrons. The BPM signal shown is the mean value of three different BPMs upstream of the profile monitor. The error bar represents the standard deviation of the three BPM readings. The measurement shows the linearity of the profile monitor signal versus beam charge, and corresponds to a charge calibration of 52 positrons per pixel output value.

282 closed, corresponding to an aperture of 5 cm. as opposed to 15 cm with
 283 the iris fully open. Figure 7 (bottom row) shows the predicted vignetting
 284 to the left, and the measured vignetting to the right. We see that there
 285 is reasonable correspondence between the predicted and measured fall-off,
 286 verifying the assumptions of the Cherenkov ring propagation used in our
 287 system description.

288

289 5.3. Resolution

290 By adding the resolution contributions from known sources, we estimate
 291 a minimum resolution of

$$\sigma_{\text{res,th}} = \sqrt{\sigma_{\text{sc,Alu}}^2 + \sigma_{\text{sc,Si}}^2 + \sigma_{\text{dof}}^2 + \sigma_{\text{opt}}^2} = 216 \text{ } \mu\text{m} \quad (6)$$

292 where $\sigma_{\text{sc,Alu}} = 122 \text{ } \mu\text{m}$ is due to scattering of the beam exit window into
 293 air; $\sigma_{\text{sc,Si}} = 11 \text{ } \mu\text{m}$ is due to scattering in upstream wafers of another dump
 294 table diagnostics; $\sigma_{\text{dof}} = 155 \text{ } \mu\text{m}$ is the depth of field error due to the air
 295 gap, calculated following Figure 2; $\sigma_{\text{opt}} = 88 \text{ } \mu\text{m}$ is the optical resolution
 296 measured with the calibration target. These contributions to the resolution
 297 are equal for both the horizontal and the vertical plane. In the horizontal
 298 plane there is an additional contribution to the resolution because the lens
 299 collects light at one side of ring, and is therefore slightly rotated by an angle
 300 θ , in order to have the wafers in the field of view. An electron trajectory will
 301 therefore be observed slightly from the side; the electron will not be imaged
 302 as a point, but as a line with width $d_{\text{gap}} \times \sin(\theta)$, where θ for our set-up is
 303 $\arctan(D/s) = \arctan(12 \text{ cm}/5.9 \text{ m}) = 20 \text{ mrad}$. The signal will therefore
 304 pick up a horizontal resolution contribution from a light distribution with
 305 full width of $5 \text{ cm} \times \sin(20 \text{ mrad}) = 1 \text{ mm}$, corresponding to an rms width
 306 of $\sigma_{\text{side}} = 1 \text{ mm} / \sqrt{12} = 290 \text{ } \mu\text{m}$. In the horizontal plane we therefore expect
 307 a larger resolution than in the vertical plane, on the order of

$$\sigma_{\text{res,th,X}} = \sqrt{\sigma_{\text{res,th}}^2 + \sigma_{\text{side}}^2} = 362 \text{ } \mu\text{m}. \quad (7)$$

308 The effective resolution of the system was measured by comparing the
 309 electron beam size measured, with a Kodak lanex screen and a second Cherenkov
 310 system. The second Cherenkov system, which we call the “NEAR” lens sys-
 311 tem, has a smaller air gap and the is lens placed close to the wafers so that
 312 the entire Cherenkov ring falls on the lens, corresponding to operation mode

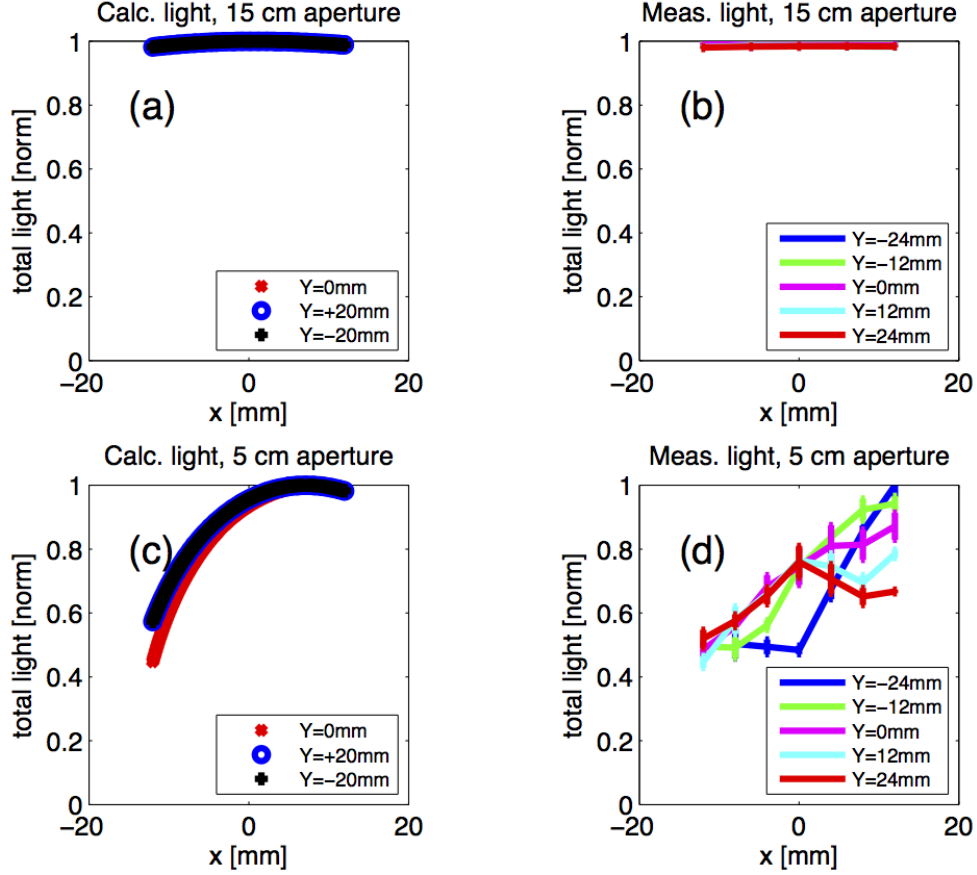


Figure 7: Light yield for the FACET spectrometer profile monitor, as function of horizontal charge position, for a set of vertical positions. The top row of plots shows light yield for the nominal profile monitor configuration, with the lens iris fully open; (a) shows the calculated light yield using Eqs. (3) and (4), (b) shows the measured light yield. We observe less than 3% variation in the light yield for any horizontal and vertical charge location, both for the calculated case and for the measured case. In comparison, the bottom row of plots shows light yield for a test configuration with the lens iris set to 1/3 of full aperture; (c) shows the calculated light yield using Eqs. (3) and (4), (d) shows the measured light yield. Both the calculated and the measured case show for this configuration a sharp fall-off in the light yield, as function of the horizontal position of the particles. The measured fall-off is in reasonable agreement with the calculated values, and indicates the validity of the ray tracing model.

313 “1” in Figure 1. This is as opposed to the main lens system described in this
 314 paper, which we call “FAR” for comparison, which operates in mode “2” in
 315 Figure 1. The electron beam size at the location of the Cherenkov wafers was
 316 varied using focusing magnets. By comparing the spot size on the different
 317 systems, the resolution of systems could be estimated. The resolution of the
 318 “FAR” system was measured to be

$$\sigma_{res,x} = 350 \mu\text{m} \pm 25 \mu\text{m}$$

$$\sigma_{res,y} = 230 \mu\text{m} \pm 20 \mu\text{m}$$

319 For the “FAR” system, the measured resolution in y is consistent with the
 320 estimate given in Eq. (6), and the measured resolution in x is consistent with
 321 the estimate given in Eq. (7). In comparison, for the “NEAR” system the
 322 resolution in both planes were measured to be

$$\sigma_{res,NEAR} = 140 \mu\text{m} \pm 20 \mu\text{m},$$

323 which is within the expected resolution from known sources for the “NEAR”
 324 system. Figure 8 illustrates the asymmetry in the “FAR” system, by com-
 325 paring a single electron beam shot, generating light on both systems. On
 326 the “NEAR” system, the measured spot size is similar in both planes, while
 327 for the “FAR” system, the measured spot size is significantly larger in the
 328 horizontal plane than in the vertical plane, as expected from the discussion
 329 above.

330

331 The main purpose of the FACET Cherenkov profile monitor is to per-
 332 form spectrometer energy measurements. The dispersion induced by the
 333 spectrometer dipole, at the nominal FACET beam energy of 20.35 GeV,
 334 is $D_0 = 62$ mm. We define the detector energy resolution as $\sigma_{res,E} =$
 335 $\sigma_{res,y}/D \times E = \sigma_{res,y}/D_0 \times E^2/E_0$. For nominal parameters the energy
 336 resolution is $\sigma_{res,y}/D_0 \times E_0 = 76$ MeV, or 0.4% of the nominal energy. The
 337 energy resolution scales with the particle energy squared, yielding better res-
 338 olution at lower energy and poorer resolution for higher energy. Figure 9
 339 displays the energy resolution as function of the particle energy E .

340

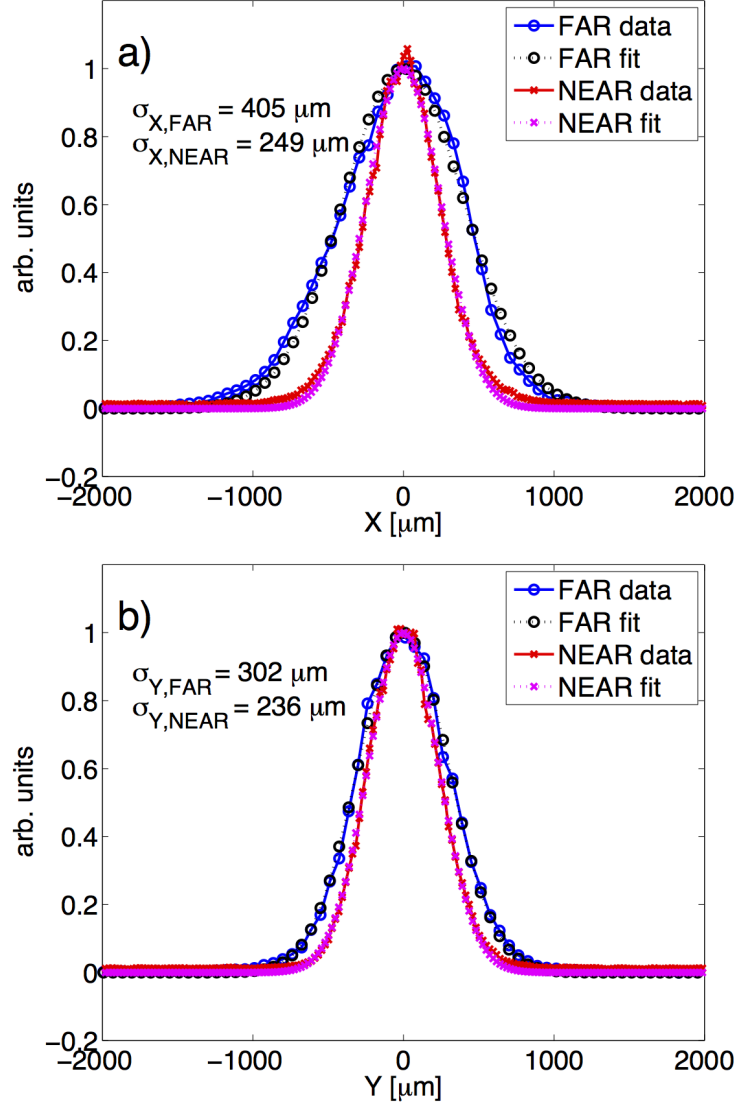


Figure 8: Example of the projected light distribution generated from a single electron shot, in both planes, for both the “FAR” system described in detail in this paper, where only a fraction of the Cherenkov ring hits the lens, and the “NEAR” system where the entire Cherenkov ring hits the lens. On the “NEAR” system, the measured spot size is similar in both planes, while for the “FAR” system, the measured spot size is significantly larger in the horizontal plane than in the vertical plane. For the “FAR” system a larger resolution in the horizontal plane is expected as the camera is viewing the air gap from a slight horizontal angle.

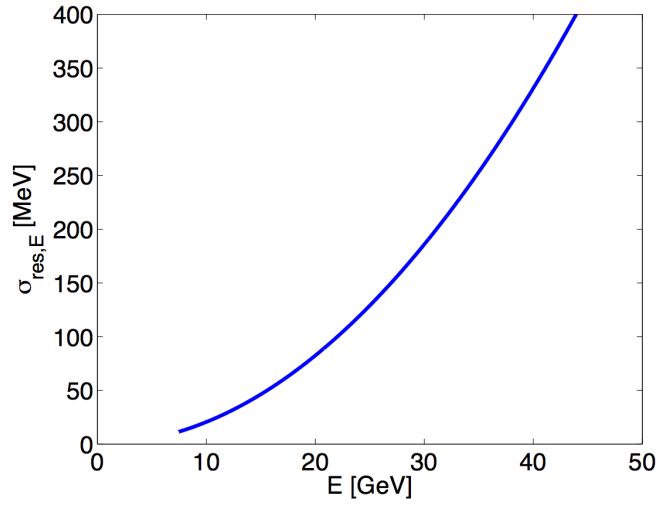


Figure 9: The detector energy resolution of the FACET Cherenkov spectrometer, as function of the particle energy. The energy resolution given here is calculated as the measured spatial resolution in the vertical plane, divided by the dispersion due the spectrometer dipole, times the particle energy. For the nominal FACET beam energy of 20.35 GeV, the energy resolution is 76 MeV, or 0.4% of the nominal energy.

341 5.4. Wafer damage

342 We have observed that the intense electron beam can create visible dam-
 343 age on the 800 μm thick silicon wafers, if enough electron pulses hit the
 344 wafers. Since visible damage affects the reflection coefficient unevenly, this
 345 may create an error in the measurement.

346 There will be a temperature increase in the Si wafers due to energy depo-
 347 sition originating from collisional losses of the electron beam in the wafers.
 348 The mean collisional losses, dE/dx_{coll} , for a 20 GeV electron passing through
 349 Silicon is 2.3 MeV $\text{cm}^2 \text{g}^{-1}$ [16]. We estimate the peak surface density of
 350 the FACET electron beam to $\hat{\sigma}_b = N/(2\pi\sigma_x\sigma_y) = 8 \times 10^{14} \text{ cm}^{-2}$ [1] where
 351 $N=2 \times 10^{10}$ is the beam charge and $\sigma_x = \sigma_y = 20 \mu\text{m}$ are the rms spot
 352 sizes. We have assumed a Gaussian beam. The specific heat capacity of
 353 Silicon at 25 $^\circ\text{C}$ and 1 atm is $C_{\text{Si}} = 0.7 \text{ J g}^{-1}\text{K}^{-1}$ [17]. A single pass of the
 354 beam through the wafers may thus lead to a peak temperature increase of
 355 $\Delta T = dE/dx_{\text{coll}} \times \hat{\sigma}_b / C_{\text{Si}} = 418 \text{ K}$. This is a significant temperature increase
 356 compared to the melting point of Si which is 1687 K, and may be a cause of
 357 the damage observed.

358 We have investigated the damage quantitatively by measuring the reflec-
 359 tivity of two wafers which have seen a different number of electron pulses
 360 in the FACET run of spring 2013. One set of wafers was inserted into the
 361 electron beam only when the FACET plasma experiment was running. The
 362 experiment had about 150 hours of beam time, running at 1 Hz for most of
 363 the time, and the wafers were exposed to a few times 10^5 pulses of up to
 364 2×10^{10} electrons. Figure 10 (upper part) shows the reflection of diffuse light
 365 on these wafers after the experiment. No visible damage was observed on
 366 this set of wafers. Another set of wafers was inserted into the electron beam
 367 when the experimental wafers were extracted, in order to use the Cherenkov
 368 monitor during beam commissioning. These wafers were exposed to a few
 369 times 10^7 pulses, occurring at up to 10 Hz. Figure 10 (lower part) shows re-
 370 flection of diffuse light on these wafers after the experiment. There is a clear
 371 mark where the beam has hit the wafers, located between pixels 450 and 500
 372 in the x -direction. Outside the core of the beam the reflectivity is reduced
 373 by up to 30-40%. The system could still be used for beam commissioning
 374 purposes even this with damage.

375

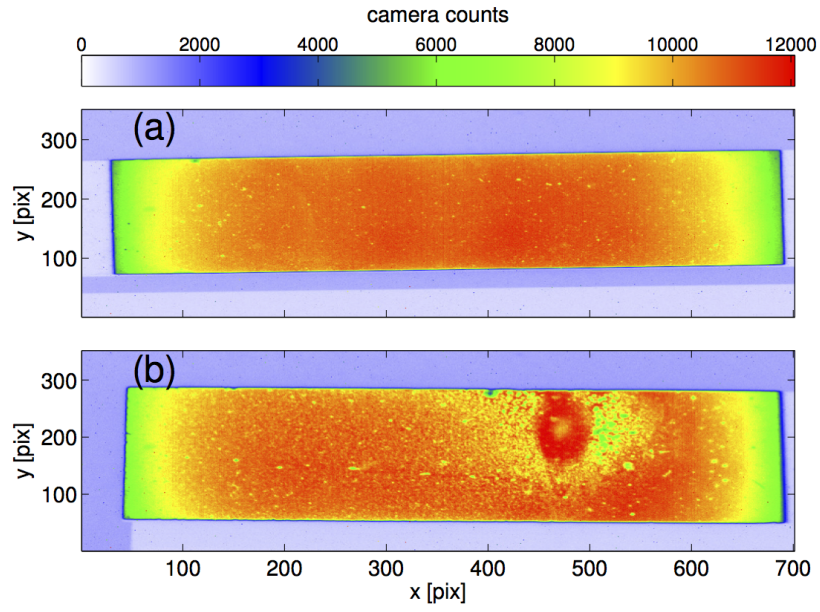


Figure 10: (a) Reflection of diffuse light off silicon wafers used for the FACET experiments in 2013. These wafers were exposed to a few times 10^5 pulses of up to 2×10^{10} electrons, and show no visible sign of degradation. (b) Reflection of diffuse light off silicon wafers which have been in the beam line during all of the FACET commissioning in 2013. These wafers were exposed to a few times 10^7 pulses of up to 2×10^{10} electrons, and shows significant degradation, which translates to reduced light yield in the affected areas.

376 6. Conclusions

377 We have discussed the principle of a transverse beam profile monitor
378 based on Cherenkov light emission in air. The light yield in this type of
379 Cherenkov monitor may be up to 100 times larger than the light yield from
380 optical transition radiation. Other key advantages of the Cherenkov monitor
381 is good robustness to radiation damage, excellent separation of incoming
382 photons and electrons, linearity with beam charge and independence of the
383 signal intensity with particle energy. The depth of field effect may give a
384 limitation on the system resolution compared to a Lanex screen. We have
385 shown that by careful design, a large field of view can be obtained, with
386 very good light coverage in the entire field of view. The system is simple
387 and robust, and easy to install, provided the beam is transported through
388 air or similar media. The silicon wafers used to reflect the Cherenkov light
389 can survive at least 10^5 pulses of up to 2×10^{10} electrons without significant
390 degradation. If the silicon wafers are hit by an order of magnitude more
391 electron pulses the wafer reflectivity may be affected, and the wafers should
392 be replaced with a new set for optimum performance.

393 7. Acknowledgments

394 We are grateful for the cooperation of the FACET operational crew for
395 help with providing the beam used for testing the system. We thank Stan-
396 ford University students Julien De Mori and Matthew Kahane for help with
397 the installation of the system, and Carl A. Lindstrøm for proofreading. Sili-
398 con wafers have been procured from WRS Materials, and we appreciate the
399 excellent service from Michelle Piffero. This work is supported by the Re-
400 search Council of Norway and the U.S. Department of Energy under contract
401 number DE-AC02-76SF00515.

- 402 [1] M. J. Hogan et al., New J. Phys. **12**, 055030 (2010)
403 [2] X. Wang et al., Nature Communications, **10**, 1988 (2013)
404 [3] A Multi-TeV Linear Collider Based on CLIC Technology: CLIC Con-
405 ceptual Design Report, CERN, Geneva (2012)
406 [4] I. Blumenfeld et al., Nature **445**, 741 (2007)
407 [5] R. Ischebeck et al., in Proceedings of PAC'07, p. 4168 (2007)

- 408 [6] M. Litos et al., *Nature* **515**, 92 (2014)
- 409 [7] R. Carr and H. Wiedemann, in *Handbook of Accelerator Physics and*
 410 *Engineering*, 3rd ed. World Scientific Publishing Co. Pte. Ltd, 2006,
 411 sec. 3.1.6, p. 214.
- 412 [8] A. Buck et al., *Rev. Sci. Instrum.*, **81**, 033301 (2010)
- 413 [9] P. A. Cherenkov, *Dok. Akad. Nauk SSSR* **2**, 451 (1934)
- 414 [10] K.P. Birch and M.J. Downs, *Metrologia* **30**, 155 (1993).
- 415 [11] K.P. Birch and M.J. Downs, *Metrologia* **31**, 315 (1994).
- 416 [12] I. Tamm, *J. Phys.(USSR)* **1**, 439 (1939)
- 417 [13] pco.edge 5.5, scientific CMOS camera,
 418 <http://www.pco.de/categories/scmos-cameras/pcoedge/>
- 419 [14] USAF Resolution Test Chart, en.wikipedia.org/wiki/1951_USAF_resolution_test_chart
- 420 [15] R. Carr and H. Wiedemann, in *Handbook of Accelerator Physics and*
 421 *Engineering*, 3rd ed. World Scientific Publishing Co. Pte. Ltd, 2006,
 422 sec. 3.3.1, p. 243.
- 423 [16] W. R. Leo, *Techniques for Nuclear and Particle Physics Experiments*,
 424 Springer (1994).
- 425 [17] National Institute of Standards and Technology,
 426 <http://webbook.nist.gov>.

Figure

[Click here to download high resolution image](#)

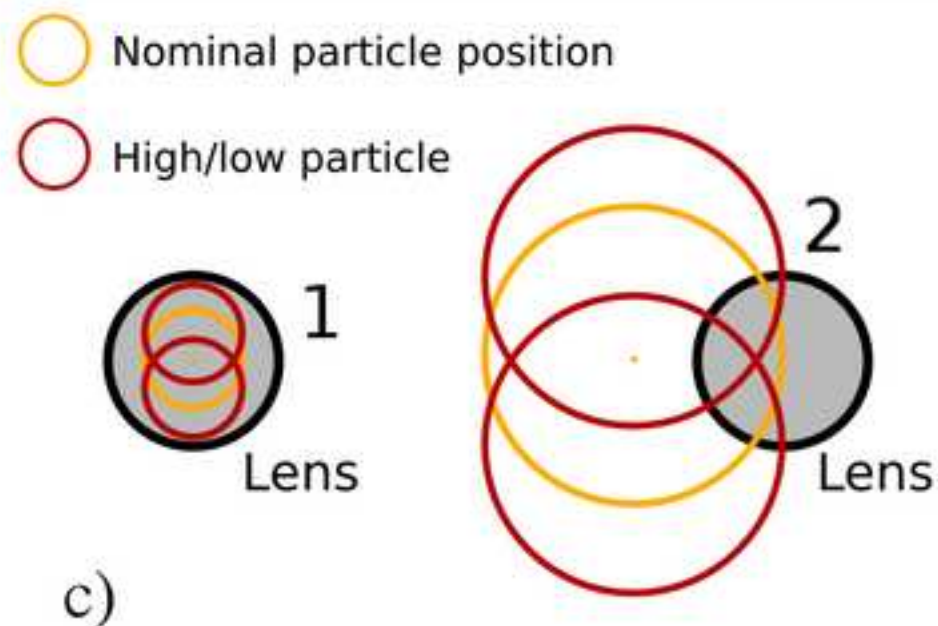
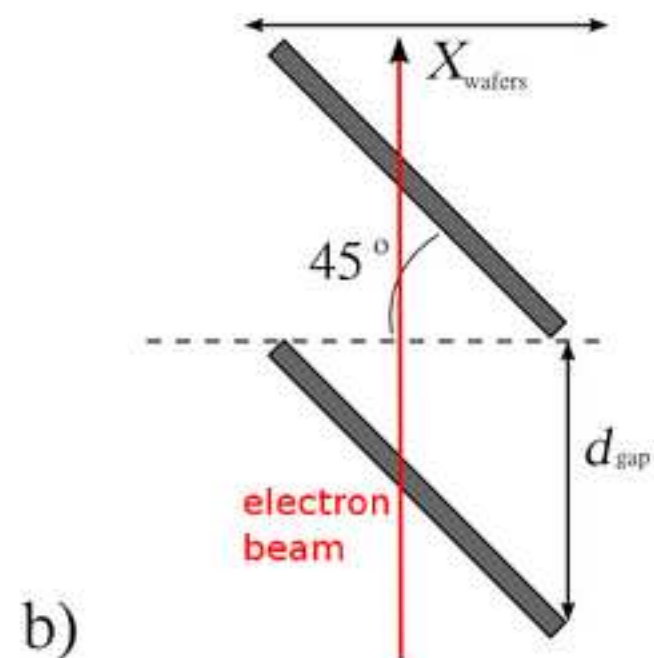
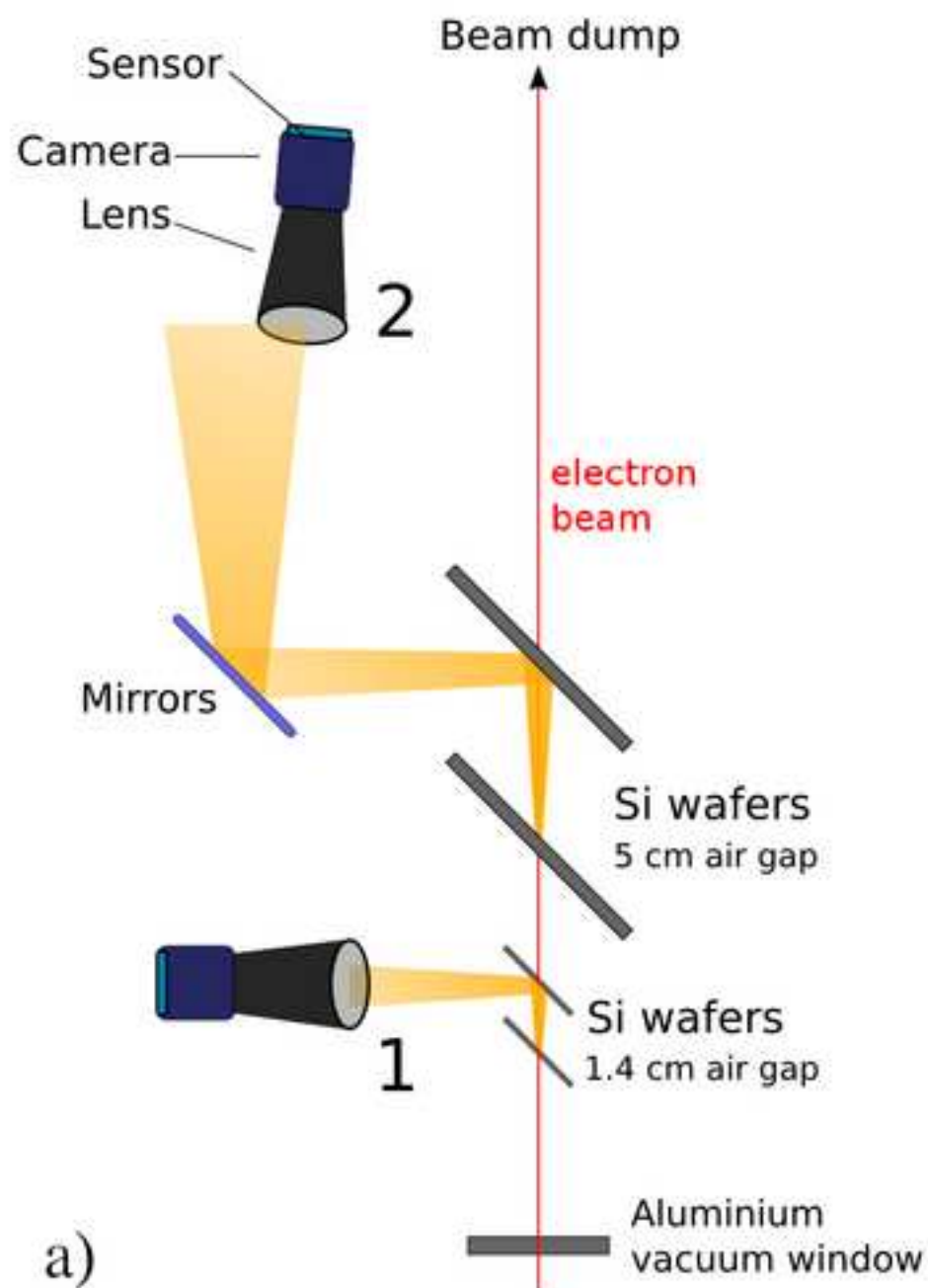


Figure
[Click here to download high resolution image](#)

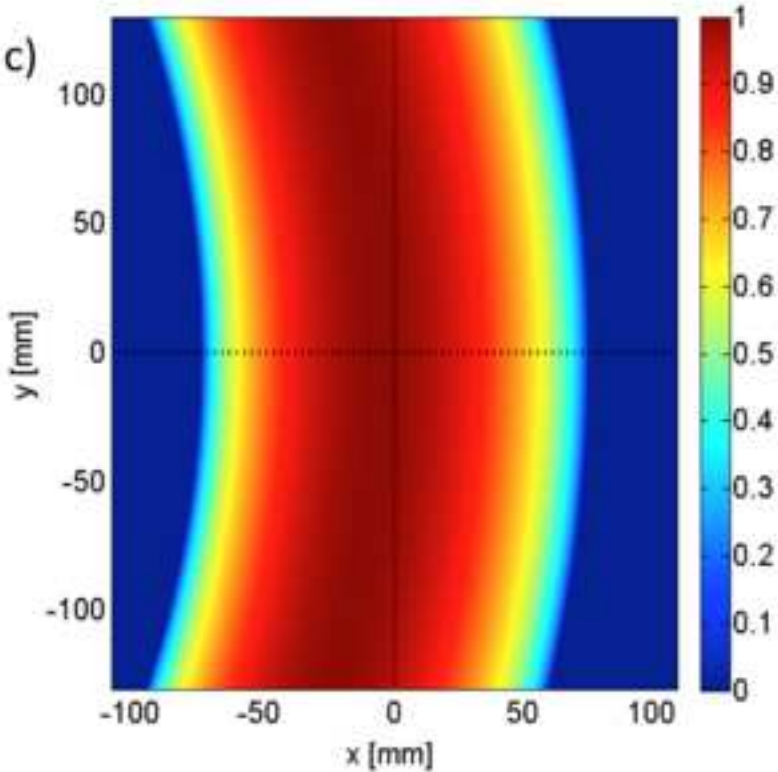
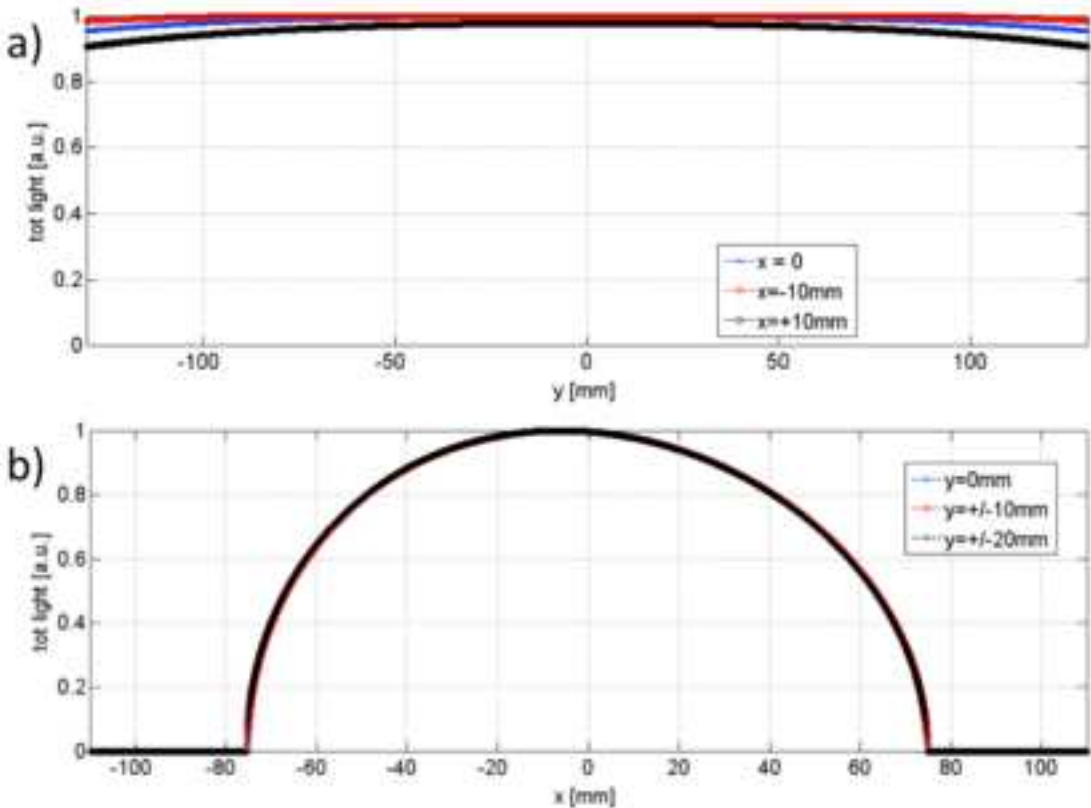


Figure
[Click here to download high resolution image](#)

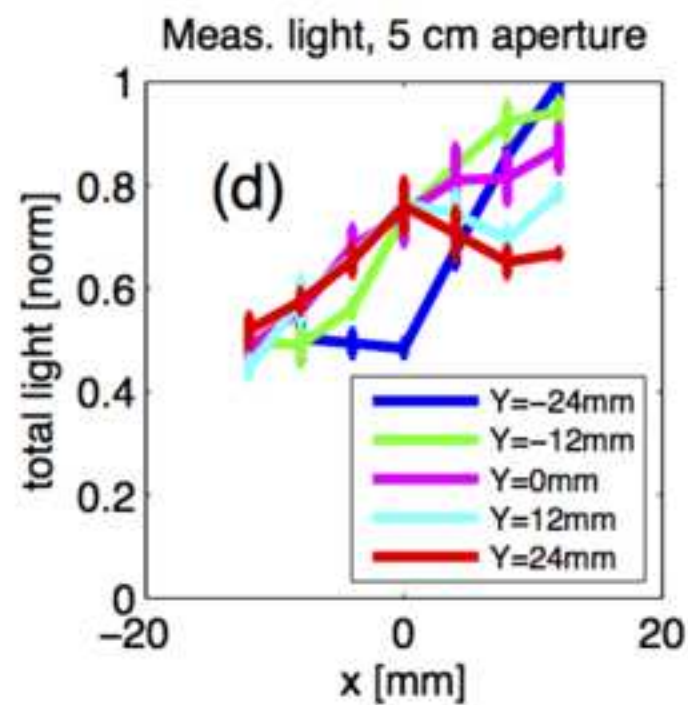
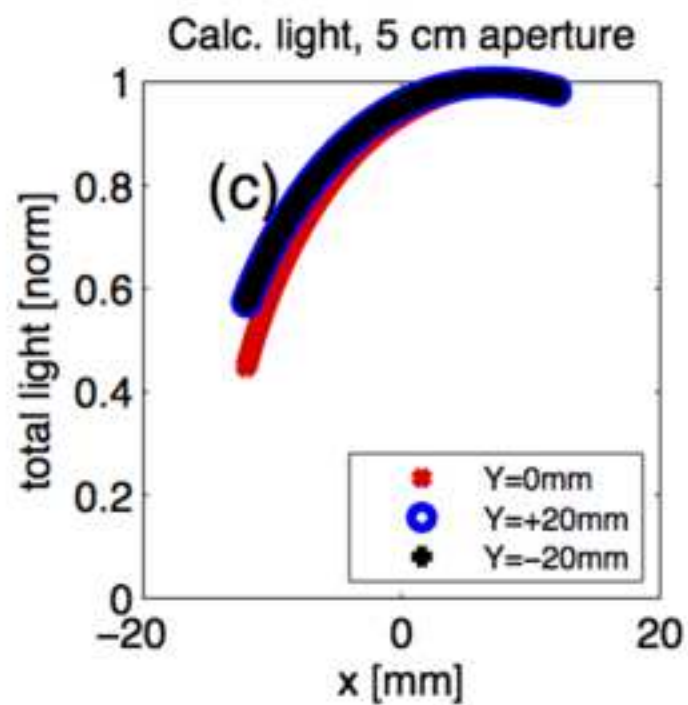
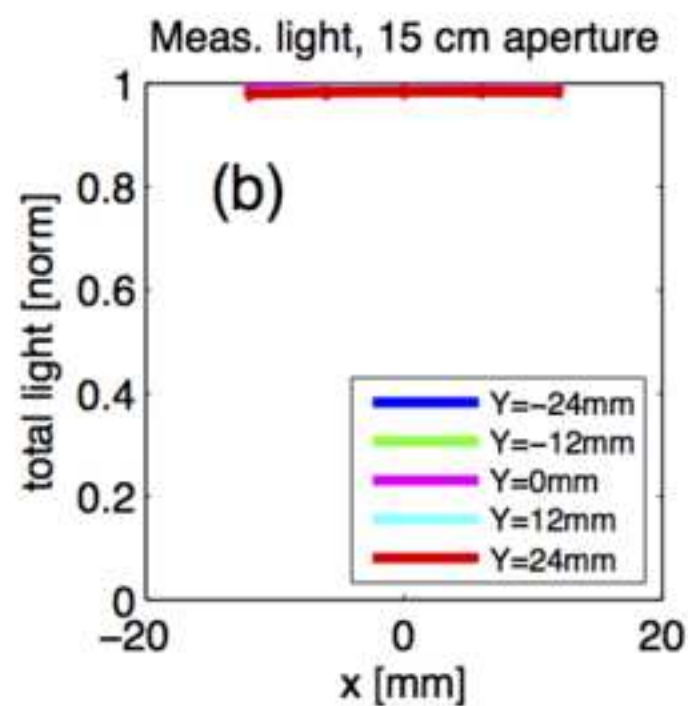
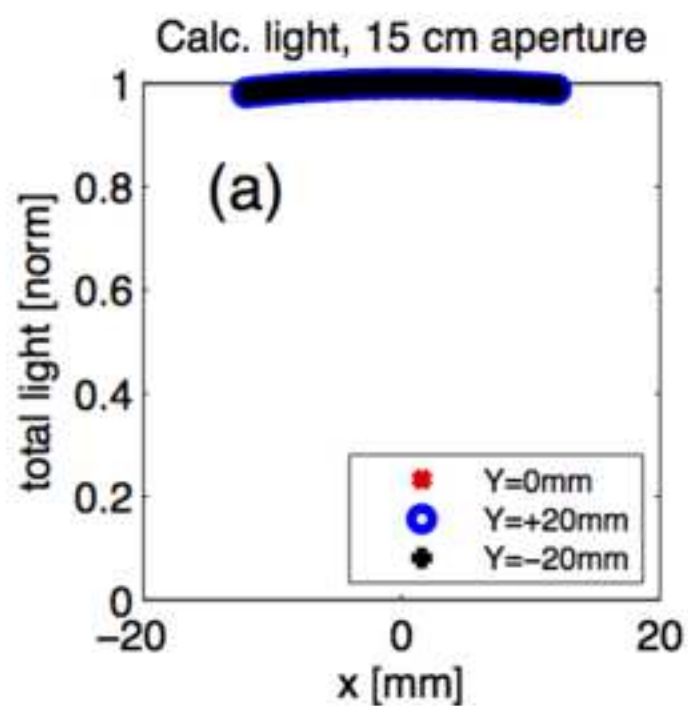


Figure
[Click here to download high resolution image](#)

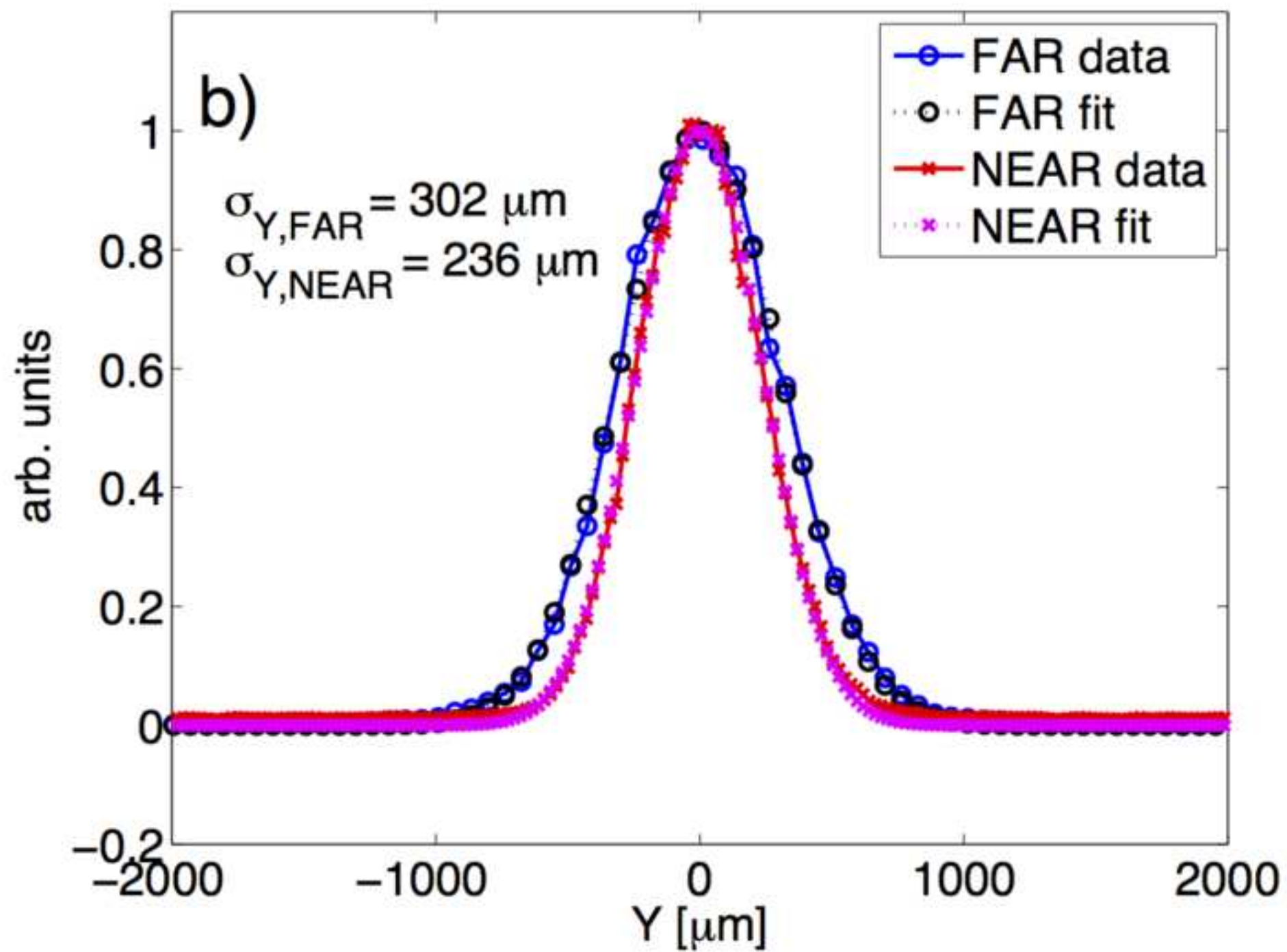


Figure
[Click here to download high resolution image](#)

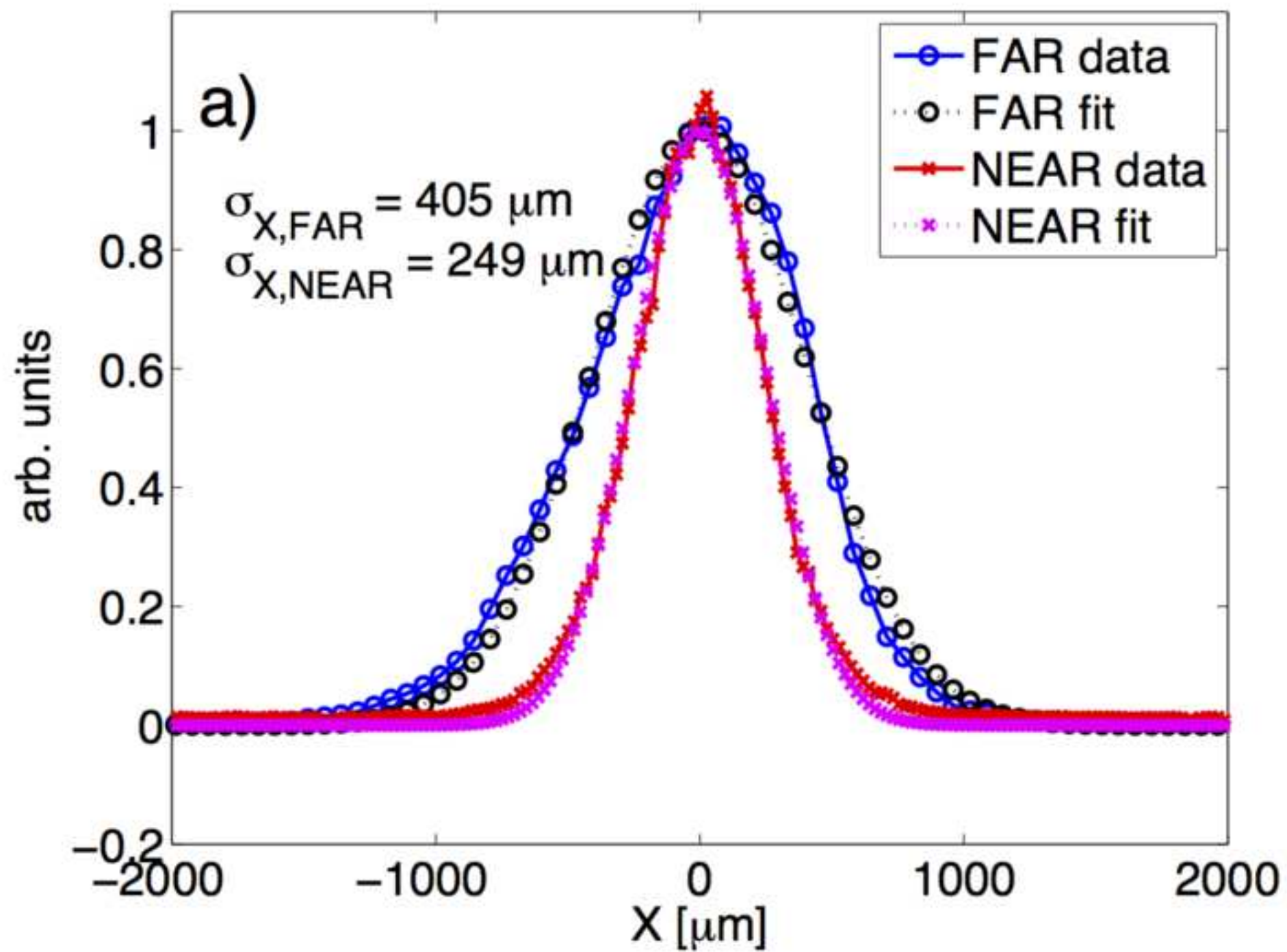
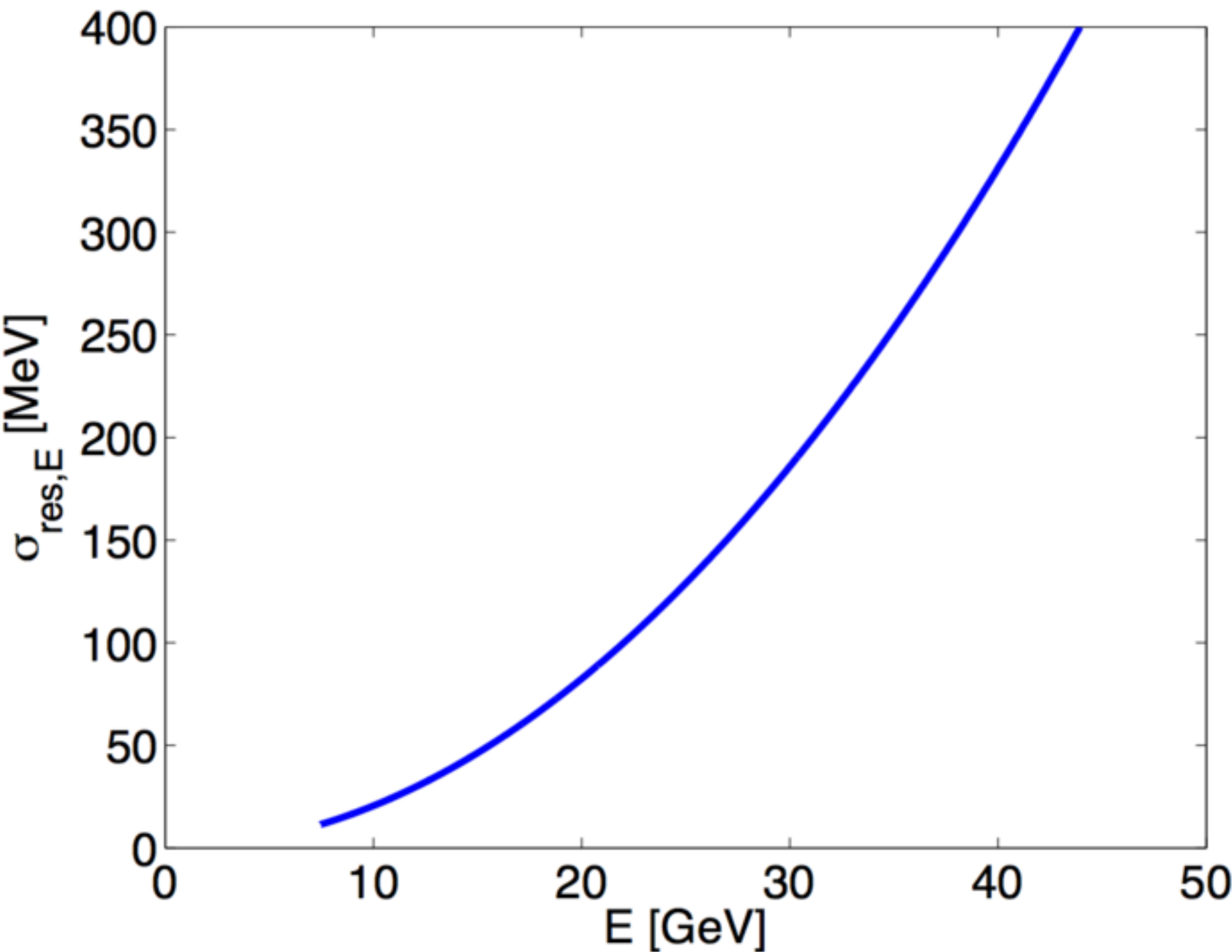
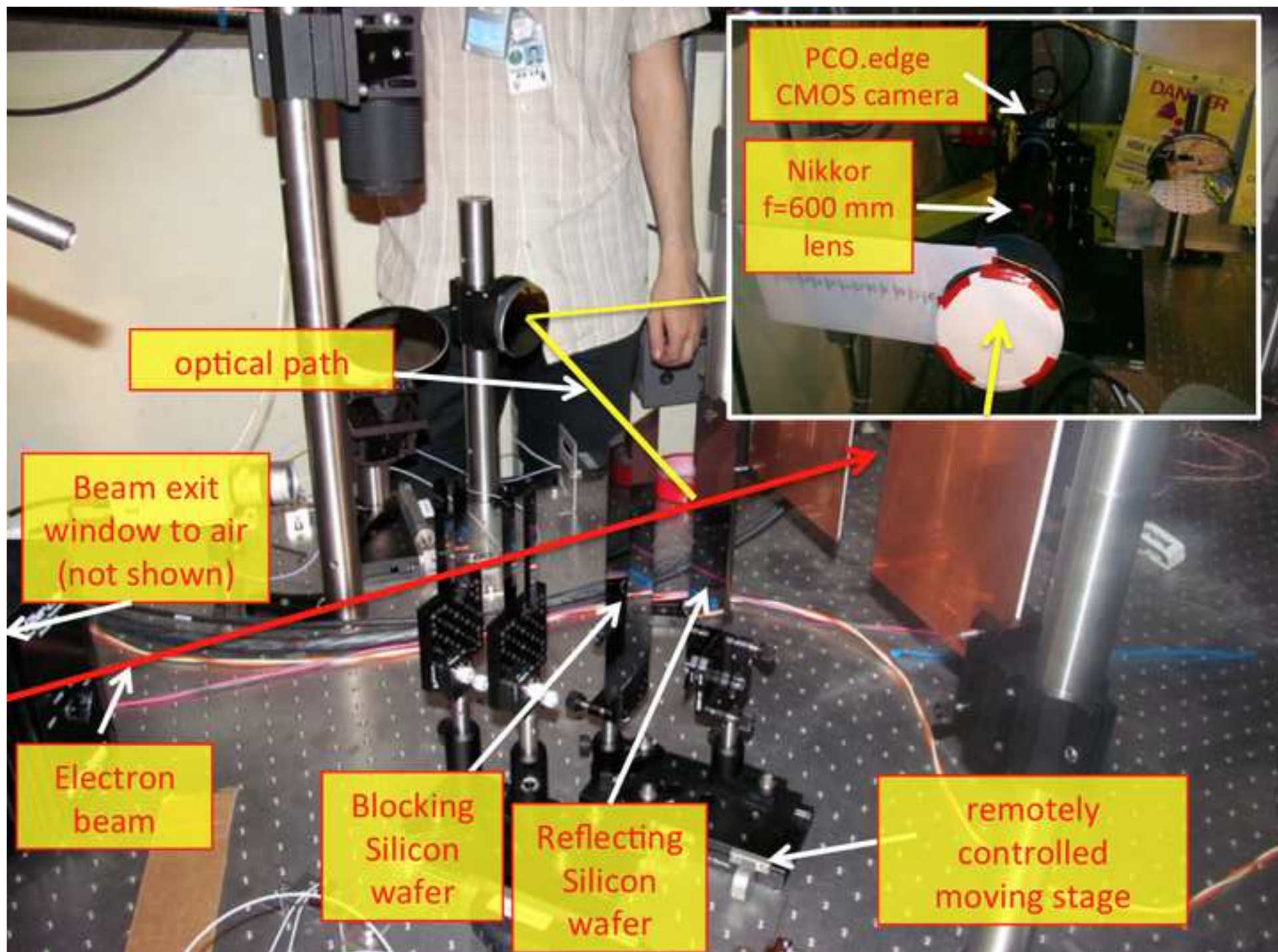


Figure
[Click here to download high resolution image](#)



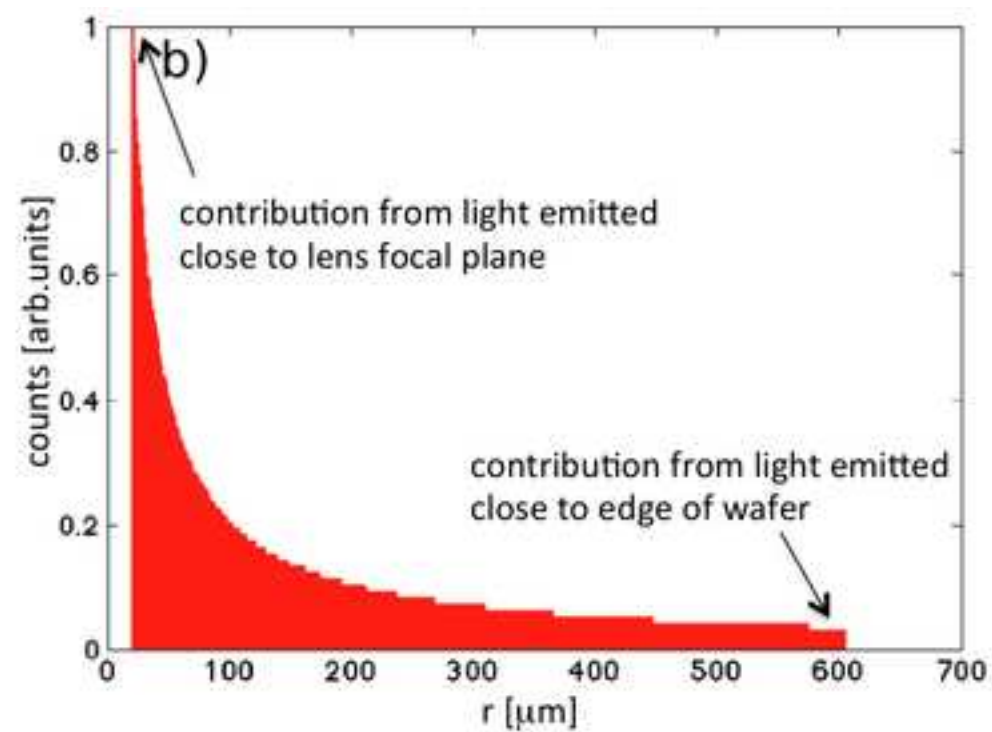
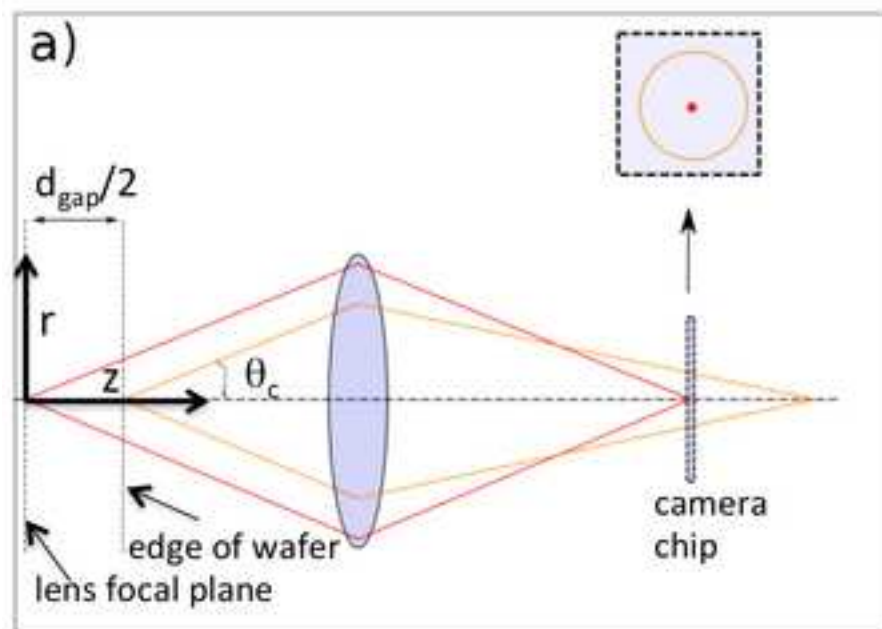
Figure

[Click here to download high resolution image](#)



Figure

[Click here to download high resolution image](#)



Figure

[Click here to download high resolution image](#)

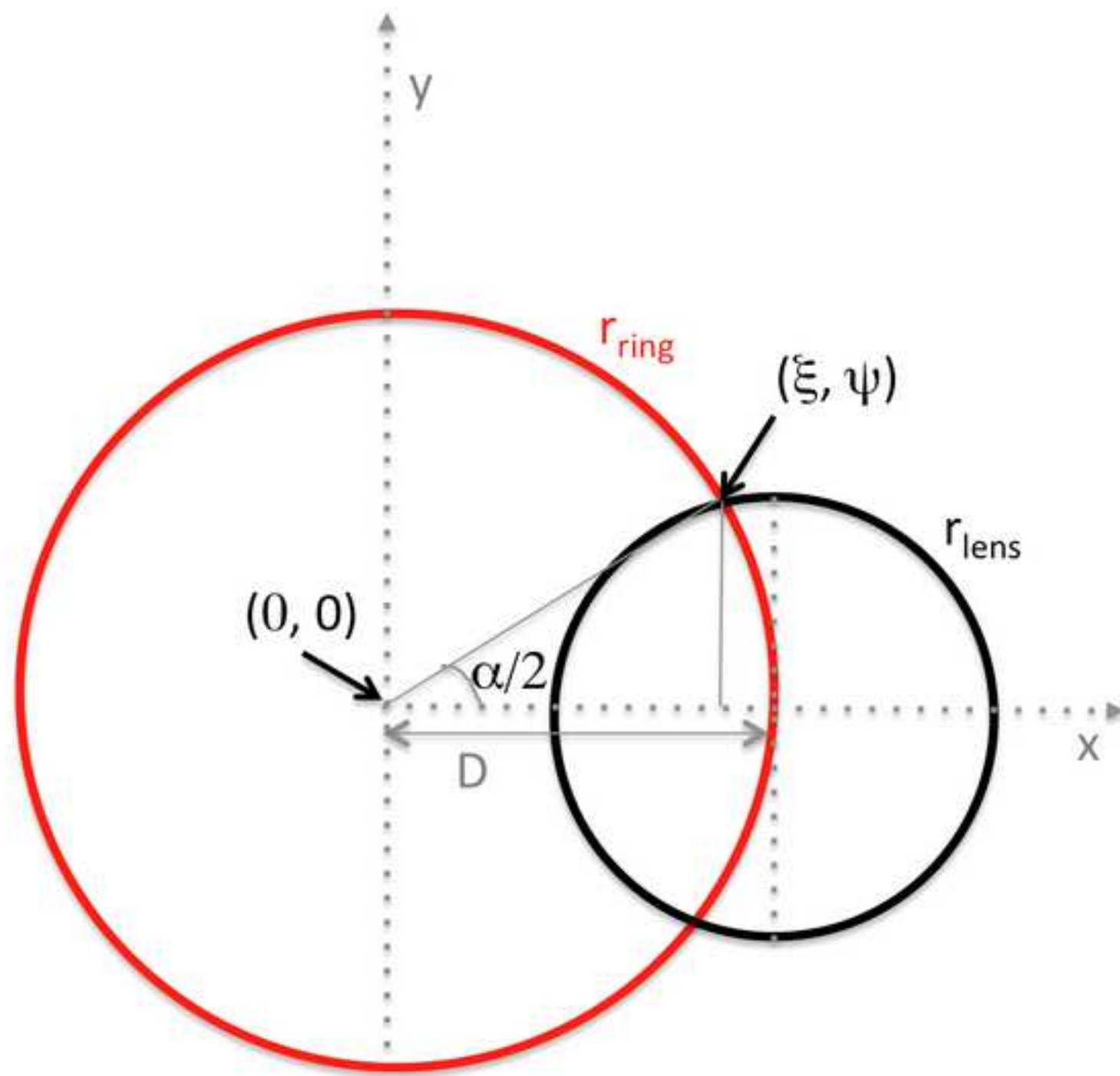
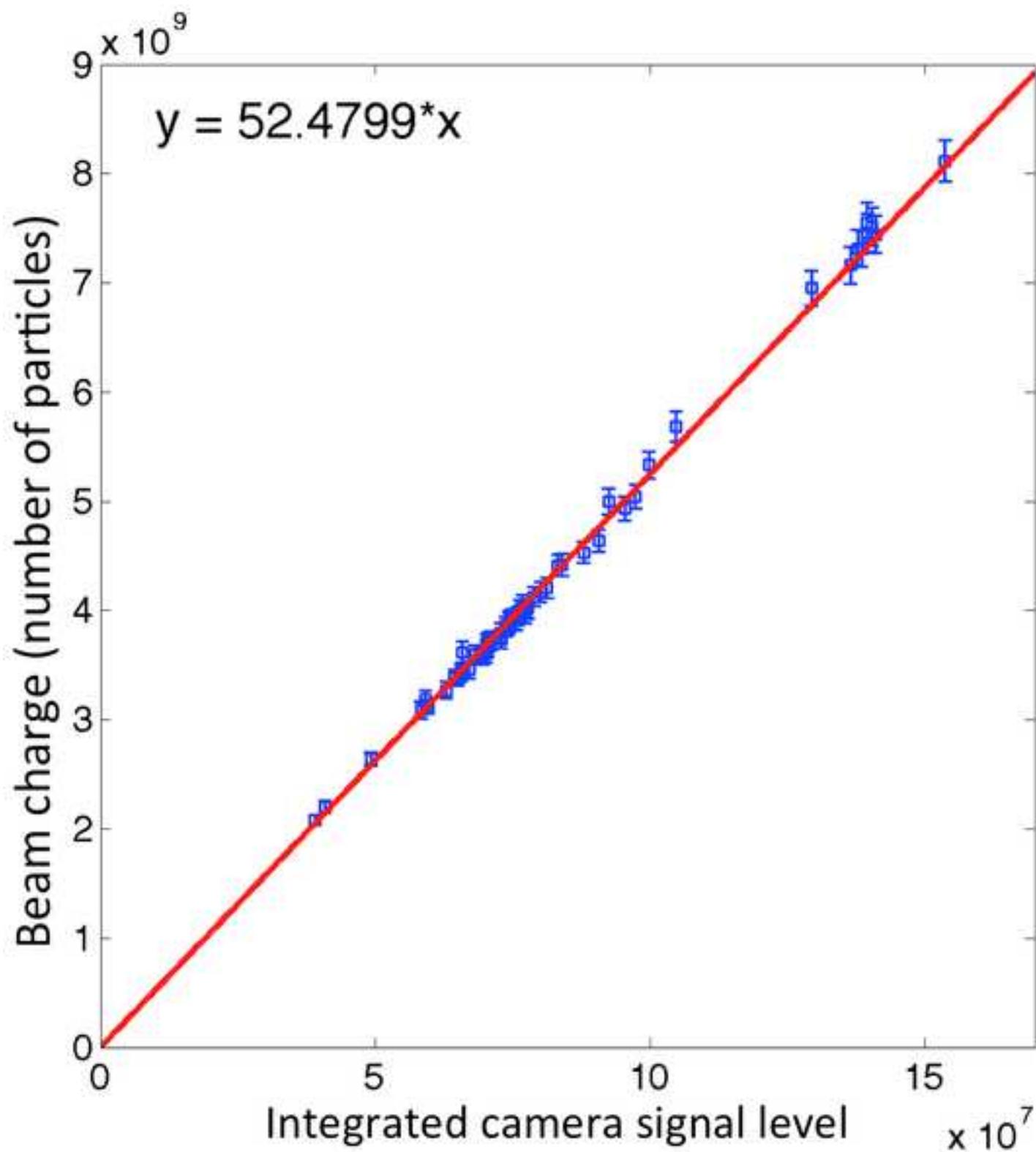


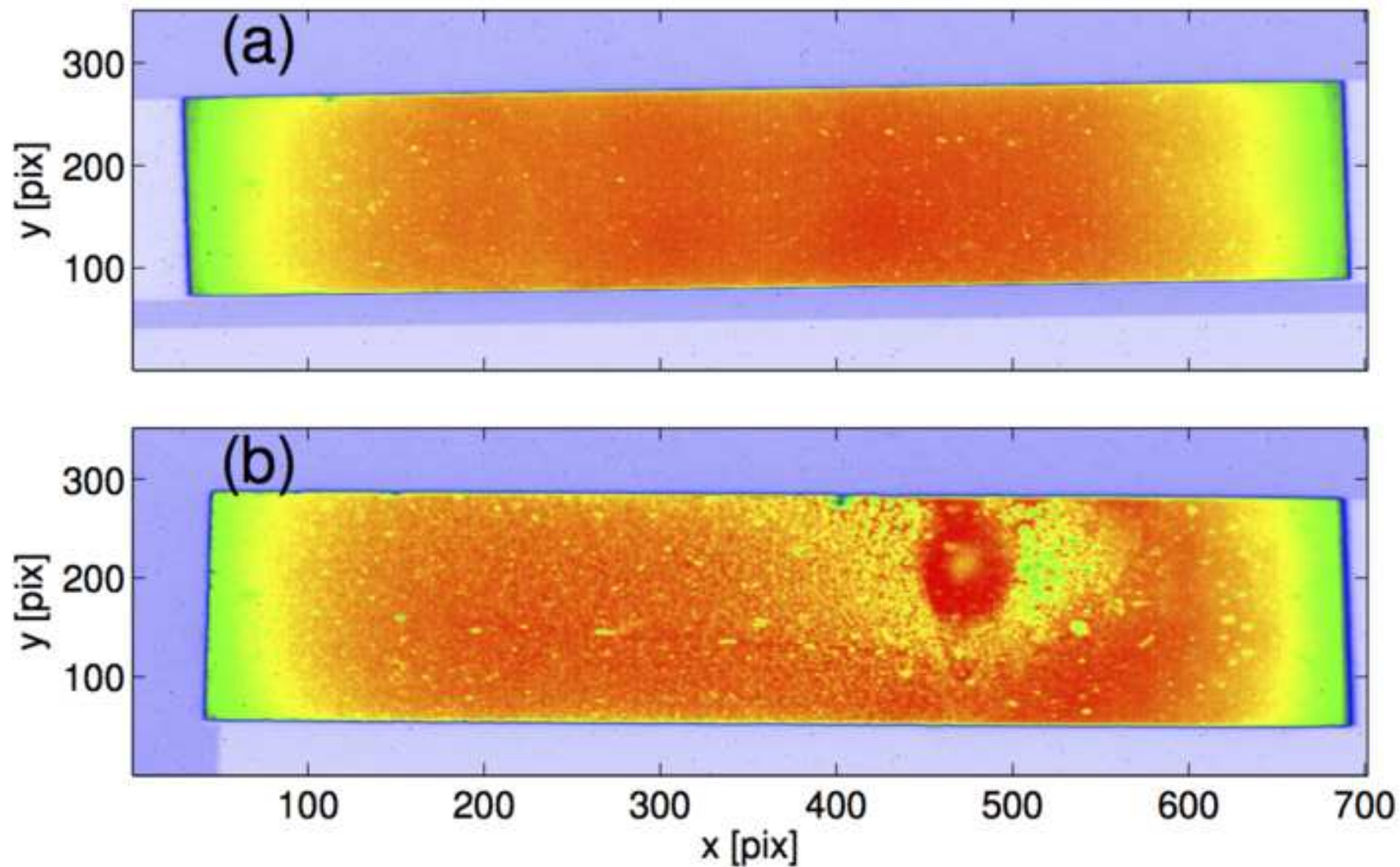
Figure
[Click here to download high resolution image](#)



Figure

[Click here to download high resolution image](#)

camera counts



Reviewers' comments:

We thank the reviewer once again for good comments, and we believe all outstanding issues have been addressed, as further discussed below.

Reviewer #1: The paper has been updated, all the comments have been taken into account a adequate answers given. I only have a few minor points to rise to the authors.

Line 87: "is the preferred material for inner detectors in particle collider experiments"

I think this is because of the particle detection properties of Silicon, there are many other materials much more radiation resistant like steel, but not suited to build a particle detector (CVD-SiC is also often used for cases like yours, but has a lower reflectivity than Si). May be this sentence should be removed. I agree on all other comments you made about silicon.

Ok, we have removed the reference to particle collider experiments.

Line 146: If you want to image the full FOV then the magnification has to be smaller-equal than $X/(2r_{\text{lens}}-2r_{\text{ring}})$ and not larger, indirectly you say

exactly that in the two explanation points just after

We agree; the \ge should be a \le to be consistent with the text. Good spot.

Line 259: "freshly installed..." -> new wafers

Ok, we simply write relatively "new wafers" instead.

Answer to question "line 264: It is stated at the beginning of the paper that diffraction is not important. For the FAR system I think that diffraction IS important for the horizontal plane as the singleelectron response is a thin vertical line on the lens, i.e. with a small horizontal angular aperture. The diffraction effect can be estimated either by simple approximation using the angular aperture and the diffraction formulas or using electro magnetic solvers. It would be nice to have this calculation included and see if it can be the source of the discrepancy."

I am not sure the answer addresses the problem. First of all I was just talking of single particle response (sometimes called PSF), for this the beam size has no role. My point is that the light is emitted over a cone (a hollow cone!) which means that on the lens you have something close to a vertical line whose thickness is

not mentioned (this was asked in one of my other questions) diffraction limits the product of the image size and the angular acceptance of the light beam. In this case the angular acceptance (for X) is just the thickness of that line divided by the distance between the source and the lens. This is entirely different from the case where you capture the full rings in which case the angular aperture is the Cherenkov angle. The reference to the OTR paper is not appropriate as it addresses a different problem which is the fact that the diffraction limit of OTR is not dominated by the $1/\gamma$ characteristic angle since there are large tails in the OTR angular distribution. OTR is eventually dominated by diffraction either at very high energies or for very small beams.

As a quick and dirty estimate the thickness of the cone is about $5\text{cm} \cdot \tan(24.2\text{mrad})/5.9\text{m} = 200\mu\text{rad}$ and assuming $\text{PSF} \cdot \text{angular_aperture} \sim \lambda$ $\text{PSF} = 1.9\text{mm}$. Of course this is a very simplified calculation that does not take into account that the light is not a line but a section of a circle (increasing the angular aperture), but I think it indicates that the diffraction may be the problem. A detailed study would need the use of ZEMAX in POP mode for example.

As for the diffraction question, we did do some estimates in the previous response. We still do not think that the diffraction effects as discussed by the referee above is the

source of the resolution discrepancy since, because as said in the previous response, the lens is in the far field, and the propagation of light from the source to the sensor is basically two times a Fourier transform, and the resolution is in this case not limited by diffraction.

However - and more importantly - the referee's comment above lead us to think about the following effect, which we believe DO explain the resolution discrepancy : the lens collects light at one side of ring, and is therefore slightly rotated to still have the wafers close to the center of the field of view. This means that it observes an electron trajectory slightly from the side, with an angle "theta". A single electron will therefore not be imaged as a point, but as a line with width $d_{\text{airgap}} * \sin(\theta)$. The angle theta is in our case about 20 mrad (slightly smaller than the 24.2 mrad since the center of the ring is 12 cm away from the center of the lens, while the radius of the ring is 14.3 cm). The light in the horizontal plane will therefore pick up resolution contributions from an object with full width of 1 mm, with an rms width of $1 \text{ mm} / \sqrt{12} = 290 \text{ um}$. This contribution is consistent with the higher resolution measured in the horizontal plane. I.e. adding the theoretical resolution and the "angle contribution" in quadrature $\sqrt{216^2 + 290^2} \text{ um} = 362 \text{ um}$ is consistent with the measured resolution reported to $350 \text{ um} \pm 25 \text{ um}$.

We added an explanation to explain this effect in the paper, and discuss that the measured resolution now is

consistent with the predictions.

Please note that this effect is a purely geometric effect, explainable by ray optics, and thus not related to diffraction. However, in order to avoid confusion about diffraction effects we do agree to remove the following sentence from paragraph 3.1 "For our experimental setup this resolution limit is larger than the diffraction limit associated with the lens aperture (see next section for numbers). ". We now do not say anything specifically about the effects of diffraction.

We thank the referee for the useful discussions that eventually lead to the solution of the resolution riddle.

Text added in the paper :

In the horizontal plane there is an additional contribution to the resolution because the lens collects light at one side of ring, and is therefore slightly rotated by an angle θ , in order to have the wafers in the field of view. An electron trajectory will therefore be observed slightly from the side, and the electron will not be imaged as a point, but as a line with length $d_{\mathrm{gap}} \times \sin(\theta)$,

where θ for our set-up is $\arctan(D/s) = \arctan(12\text{ cm}/5.9\text{ m}) = 20\text{ mrad}$. The light in the horizontal plane will therefore pick up a resolution contribution from an light distribution with full width of $5\text{ cm} \times \sin(20\text{ mrad}) = 1\text{ mm}$, corresponding to an rms width of $\sigma_{\text{side}} = 1\text{ mm} / \sqrt{12} = 290\text{ }\mu\text{m}$. In the horizontal plane we therefore expect a larger resolution, on the order of

$$\sigma_{\text{res,th,X}} = \sqrt{\sigma_{\text{res,th}}^2 + \sigma_{\text{side}}^2} = 362\text{ }\mu\text{m}.$$

\label{eq:cher_th_res_X}

We also added to the picture text
 "For the "FAR" system a larger resolution in the horizontal plane is expected as the camera is viewing the air gap from a slight horizontal angle."

answer to question "Line 290: Thermal load estimations should be included, at least for the single shot case (power deposition density, temperature increase etc.). It would be interesting also to know

why silicon wafers are used and a list of possible other materials with pro and cons from the resolution and thermal point of views."

I think you could easily calculate the ΔT for a single shot ($\Delta T(r) = N(r) dE/dx / c_v$ with $N(r)$ the particle density [e^- / m^2] dE/dx the energy deposition [$J m^2 / kg$] and c_v the specific heat [$J / Kg / K$]) The value of $\Delta T(0)$ for silicon would ver indicative of what thermal problem you have on your targets.

A temperature gradient can also induce deformation of the downstream target that will then act as a focusing/defocusing mirror affecting your measurement (deformation of the downstream target can also be the cause of the horizontal resolution).

This is a good suggestion. The total dE/dx , which is about 1000 MeV cm²/g, is dominated by Bremsstrahlung. We believe the energy lost to Bremsstrahlung will mostly escape the wafers, since the Wafer thickness (< 1mm) is much smaller than the Si radiation length (9.4 cm), and thus not contribute to the energy deposition in the wafer. We therefore use as basis for the calculation the energy deposition dE/dx for collisional losses, which for 20 GeV e^- in Si amounts to 2.3 MeV cm²/g [Leo]. Taking the best estimate for the smallest spot size of the FACET beam as observed in the experiments, which is about 20 x 20 μm^2 , combined with the beam charge of $2e^{10}e$, we get a peak surface charge density of $n_b = 2e^{10}/(2\pi)/(20e^{-4})^2 e^- / cm^2 = 8e^{14} e^- / cm^2$. Combining this with the specific heat

capacity of Si, we get an estimated peak Si temperature increase of about 400 K. This is on the order of the Si melting point of 1400 K, for a single shot. This is not the typical shot the wafers experiences, and is a worst case scenario. We have added a paragraph with this explanation in the section discussing the Si damage.

Actual text (inserted just before "We have investigated quantitatively...") with line shift afterwards :

There will be a temperature increase in the Si wafers due to energy deposition originating from collisional losses of the electron beam in the wafers. The mean collisional losses, dE/dx_{coll} , for a 20 GeV electron passing through Silicon is $2.3 \text{ MeV cm}^2 \text{ g}^{-1}$ [\cite{CHER_LEO_dEdx}](#). Our best estimate for the peak surface density of the FACET electron beam is $\hat{\sigma}_b = N/(2\pi\sigma_x\sigma_y) = 8 \times 10^{14} \text{ cm}^{-2}$ [\cite{CHER_HOG_NJP}](#) where $N = 2 \times 10^{10}$ is the beam charge and $\sigma_x = \sigma_y = 20 \text{ }\mu\text{m}$ are the rms spot sizes. We have assumed a Gaussian beam. The specific heat capacity of Silicon at 25°C and 1 atm is $C_{\mathrm{Si}} = 0.7 \text{ J g}^{-1} \text{ K}^{-1}$ [\cite{CHER_NIST_HEAT}](#). A single pass of the beam through the wafers

may thus lead to a peak temperature increase of $\Delta T = \hat{\sigma}_b \times dE/dx_{\text{coll}} \times C_{\text{Si}}$
 $= 418 \text{ K}$. This is a significant temperature increase compared to the melting point of Si which is 1687 K, and may be a cause of the damage observed.

Line 35 & figure 9: It looks like where the beam hits the reflectivity is increased? actually it looks like it is increased in some points/radii and decreased elsewhere (decreased in the core, increased in a ring just adjacent to the core then decreased again), looks weird. Surely not what is observed with the degradation of OTR screens at least.

We agree that what you describe is the observed effect of the damage; the reflectivity is reduced around the area where the core beam hits. This we say in the paper already. The precise physics of the damage formation, even though we have now shown it may be linked to temperature increase, is not clear, and thus we don't expect to be able to predict the exact damage pattern. We are not sure if there is a point to add more text with details about the damage pattern, as the damage pattern is already visible from the figure. Our main point, which is clearly stated already, is that the wafers should ideally be replaced before such damage occurs ($> 10^6$ pulses in

our case), in order to keep a constant light yield across the surface.

I understand that you may consider the last two points beyond the scope of your work, but you can not claim that diffraction is not a problem if you do not estimate its effect correctly so you may just revise that statement. For the second point I really think it is really simple to address and it would improve understanding the problem.

We believe the paper is now in a good state, having addressed both the resolution riddle, and also commented on the magnitude of Silicon wafer heating.

On our own initiative we have made one more modification to the paper : we have added a graph of the data for the charge calibration. (new Figure 6).

LaTeX Source Files

[Click here to download LaTeX Source Files: cherenkov_spectro.tex](#)